Observations of Extreme Short-Term Precipitation Associated with Supercells and Mesovortices📎

ERIK R. NIELSEN AND RUSS S. SCHUMACHER

Department of Atmospheric Science, Colorado State University, Fort Collins, Colorado

ABSTRACT

Extreme hourly rainfall accumulations (e.g., exceeding $75 \, \mathrm{mm \, h^{-1}}$) in several noteworthy flash flood events have suggested that the most intense accumulations were attendant with discrete mesoscale rotation or rotation embedded within larger organized systems. This research aims to explore how often extreme short-term rain rates in the United States are associated with storm-scale or mesoscale vortices. Five years of METAR observations and three years of Stage-IV analyses were obtained and filtered for hourly accumulations over 75 and 100 mm, respectively, clustered into events, and subjectively identified for rotation. The distribution of the short-term, locally extreme events shows the majority of the events were located along the Atlantic and Gulf of Mexico coastlines with additional events occurring in the central plains and into the Midwest. Nearly 50% of the cases were associated with low-level rotation in high-precipitation supercells or mesoscale vortices embedded in organized storm modes. Rotation events occurred more clearly in the warm sector, while nonrotation events tended to occur along a surface boundary. The rotation events tended to produce higher hourly accumulations over a larger region, but were associated with somewhat stronger synoptic-to-mesoscale forcing for ascent and more total column moisture. These results support recent modeling results suggesting that rotationally induced dynamic vertical pressure perturbations should not be ignored when it comes to extreme precipitation and can potentially enhance the short-term rain rates.

1. Introduction

Flash flooding continues to pose a substantial threat to life, property, and infrastructure throughout the United States. Even with increased societal awareness and civil mitigation, there has been no appreciable decrease in the number of flash flood fatalities in recent years (Ashley and Ashley 2008; Špitalar et al. 2014; Terti et al. 2017). Since 2003, flash flooding has been responsible for 10% of all weather-related fatalities and 20% of all weather-related property and crop-related damages in the United States, with 2015–17 being the three most deadly of the last 15 years (NWS 2018). Flash flooding differs from slow-rise flooding, such as riverine flooding, in that the rise of water is, by definition,[1] rapid and presents a particular danger to people in cars (e.g., Ashley and Ashley 2008; Maples and Tiefenbacher 2009; Sharif et al. 2015; Terti et al. 2017) or in situations with inadequate structural protection and notification methods (e.g., Špitalar et al. 2014; Terti et al. 2017).

While the rapid rise in water is related to many static and nonstatic hydrologic characteristics including topography, soil moisture, and catchment specific runoff dynamics (e.g., Costa 1987; Hapuarachchi et al. 2011; Saharia et al. 2017), the accurate prediction of the location, amount, and rate of rainfall is essential to correctly infer the hydrologic impacts and inform the decision-making process, especially when catchment dynamics and human decision making process have similar response times (e.g., Creutin et al. 2009). While

---

📎 Supplemental information related to this paper is available at the Journals Online website: https://doi.org/10.1175/MWR-D-19-0146.s1.

Corresponding author: Erik Nielsen, erik.nielsen@colostate.edu

---

[1] Defined by the National Weather Service (NWS 2017) as "a damaging and life-threatening, rapid rise of water into a normally dry area beginning within minutes to multiple hours of the causative event (e.g., intense rainfall, dam failure, ice jam)."

the numerical forecasting and real-time estimation of extreme rainfall remains a challenge within the weather community (e.g., Fritsch and Carbone 2004; Novak et al. 2011; Zhang et al. 2016), forecasting advances are continually being made to improve the identification of flash flooding potential on multiday (e.g., Herman and Schumacher 2018c,a) and nowcasting time scales (e.g., Gourley et al. 2017).

Not surprisingly, the longer and harder it rains, the higher the rainfall accumulation a location experiences. Events have occurred where either the average short-term rainfall rate (e.g., Smith et al. 2001; Hitchens and Brooks 2013), duration/quasi-stationarity of the storms (e.g., Schumacher and Johnson 2005, 2009; Nielsen et al. 2016b), or long-term combination of the two (e.g., NWS 1999, 2011; Gochis et al. 2015) led to the extreme accumulation and attendant flash flooding. The ingredients for extreme rainfall are, broadly, well known (e.g., Doswell et al. 1996) and allow for the isolation of the synoptic-to-mesoscale ingredients that are conducive for flash flooding. Within the framework established by Doswell et al. (1996), the instantaneous rain rate R can be thought of as the product of the ascent rate w; water vapor mixing ratio of the rising air q; and the precipitation efficiency E, a term that relates water vapor inflow to rainfall rate (i.e., $R = Ewq$). The rain rate seen by a specific location is known to be an important factor for runoff, soil erosion, and the resulting flood impacts, with the detrimental effects increasing for the more intense rainfall rates (e.g., Kandel et al. 2004; Mohamadi and Kavian 2015), which, in turn, can accelerate the resulting flash flood response (e.g., Kelsch et al. 2001; Kelsch 2001). For these reasons, it is important to investigate how often extreme rain rates are maintained and the meteorological conditions that support such convective systems.

Recent observational studies (Smith et al. 2001; Duda and Gallus 2010; Hitchens and Brooks 2013) have shown that extreme rainfall rates can be produced and maintained by supercell thunderstorms and other meso-γ-scale rotation,[2] despite the notion that such storms generally do not produce extreme rainfall because of low precipitation efficiency (e.g., Marwitz 1972; Foote and Fankhauser 1973; Browning 1977). Furthermore, historical studies have shown that supercells and hailstorms have been responsible for some of the most intense flash floods in U.S. history (e.g., Smith et al. 2018, 2019) and some world record rainfall accumulations (e.g., Dalrymple 1937). The apparent conflicting results between the low

precipitation efficiency arguments and the observations of supercells producing extreme rainfall has been postulated to be explained by the strong rotational dynamics that are present in supercells and mesovortices, which can serve as an additional source of positive vertical momentum (e.g., Doswell et al. 1996). The characterization and impact of these dynamic forces on supercells are discussed in length in several studies (e.g., Rotunno and Klemp 1982, 1985; Klemp 1987; Markowski and Richardson 2010). While the full derivation will not be shown here for the sake of brevity, the vertical pressure perturbations p' that leads to these nonbuoyant dynamic accelerations can be characterized, following Markowski and Richardson (2010), for well-behaved, storm-scale, and incompressible flows as

$$p' \propto \underbrace{\underbrace{e_{ij}'^2 - \frac{1}{2}|\boldsymbol{\omega}'|^2}_{\text{splat}\qquad\text{spin}}}_{\text{Nonlinear Dynamic }(p'_{\text{DNL}})} + \underbrace{2\mathbf{S}\cdot\nabla_h w'}_{\text{Linear Dynamic }(p'_{\text{DL}})} - \underbrace{\frac{\partial B}{\partial z}}_{\text{Buoyant }(p'_B)},$$

(1)

where $\boldsymbol{\omega}$ is the total vorticity of the perturbation wind, B is buoyancy, e_{ij} is the deformation tensor, w is vertical motion, and $\mathbf{S}$ is the mean environmental wind shear vector. The "spin" term of the nonlinear dynamic term implies that rotation, regardless of the direction, will result in a negative pressure perturbation. Additionally, the pressure perturbation scales with the intensity of the storm-scale rotation [Eq. (1)]. Thus, the vertical distribution of the rotation determines whether the resulting nonlinear dynamic acceleration is directed upward or downward (e.g., Klemp and Rotunno 1983). Generally, in developed supercell storms, the rotation is maximized at midlevels, which results in an upward directed dynamic acceleration and an additional nonbuoyant source of positive vertical momentum.

Investigating the influence of these rotationally induced dynamic accelerations on extreme rainfall, Nielsen and Schumacher (2018, hereafter NS18) showed that the development of meso-γ-scale rotation in convective systems associated with intense 0–1 km shear can dynamically, through the nonlinear dynamic term discussed above, enhance the storm's low-level updrafts and aid in lifting convectively inhibited parcels that still contain moisture and convective available potential energy (CAPE; Fig. 1). This rain rate enhancement was demonstrated in the NS18 with three numerical simulations where the simulations with higher 0–1 km shear and corresponding increased rotation produced significantly larger rainfall totals (Fig. 1b). The accelerations associated with the nonlinear dynamic accelerations were

---

[2] Hereafter "rotation" will refer to meso-γ-scale rotation around a vertical axis.
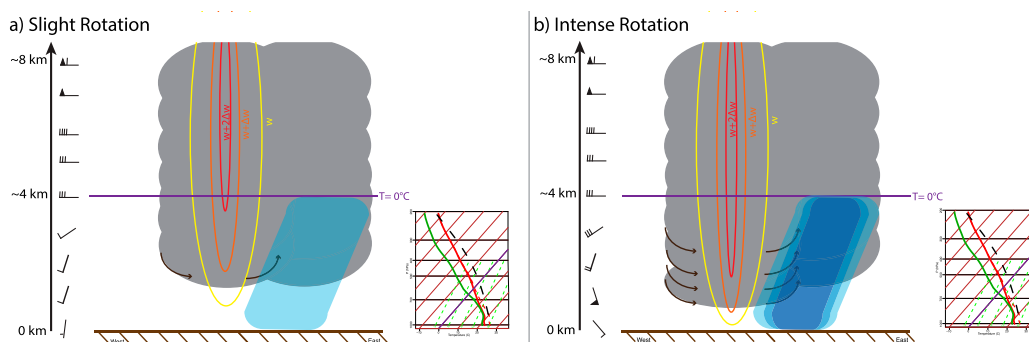
FIG. 1. Schematic summarizing the precipitation enhancement mechanism discussed in NS18. Figure shows an idealized storm system with (a) slight and (b) intense rotation in the same thermodynamic environment, which is denoted by the inset skew T–log$p$ in each panel and has the same plotting scheme as Fig. 3. Representative kinematic profile for each case is depicted by the wind barbs following the normal convention on the left side of each panel. Rotation is indicated by arrows, with the strength proportionate to number of arrows. Blue shading represents precipitation intensity, which increases as the blue shade darkens. Warm contours represent updraft velocity contours, and purple contour represents freezing level.

solved for numerically and, despite the relatively shallow nature of the rotation (i.e., maximized below ~2.0 km, see Fig. 14 of NS18), significantly enhanced the low-level updrafts of the convective system. Furthermore, downward directed accelerations are seen above the level of maximum rotation, but it did not appear to greatly affect the overall vertical motion of the system, as the overall vertical mass flux throughout the column in the simulations still increased with the amount of low-level rotation/dynamical acceleration. This is likely because low-level dynamically enhanced updrafts lifted parcels past their levels of free convection (LFCs) and thermodynamic buoyancy was now acting in concert with the dynamic accelerations. Overall, examining these two dynamically induced effects (i.e., lowering and enhancement of the low-level updrafts) within the framework established by Doswell et al. (1996) (i.e., $R = Ewq$), it becomes clear that the presence of dynamic accelerations associated with rotation can potentially enhance the observed rain rates, since both the strength of the ascent rate and water vapor mixing ratio of the air ingested by the storm are potentially increased, all else being equal (Fig. 1).

As discussed from a more societal impact point of view in NS18, the presence of strong, dynamically forced updrafts at low levels is also a favorable condition for tornadogenesis (e.g., Markowski and Richardson 2014). The ability for rotation to enhance precipitation and the parallel of tornado threat serves as a dynamic explanation for the frequency of concurrent, collocated tornado and flash flood events (TORFF events, Nielsen et al. 2015) in various storm modes, both single-cell and multicell, without a clear reliance on storm duration or motion (Bunkers and Doswell 2016; Nielsen et al. 2016a). Such concurrent, collocated scenarios elevate the threat to life and property, since the recommended lifesaving actions

for a tornado and flash flood scenario are contradictory[3] and further motivates the need to examine the effects of meso-γ-scale rotation on rainfall processes.

The numerical simulations performed in NS18 were based upon a single extreme rainfall producing event that occurred in south-central Texas on 30–31 October 2015. While many other such events have been anecdotally noted by the authors, analyzed in a limited fashion by Smith et al. (2001) and Hitchens and Brooks (2013), and tangentially examined in the context of TORFF events (e.g., Nielsen et al. 2015; Nielsen 2019), a more robust examination of the distribution of extreme, short-term rainfall accumulations events has not been undertaken recently for the United States. This, combined with the recent results of NS18, provide the motivation to examine such extreme rainfall events for the presence of meso-γ-scale rotation. The ultimate goal is to provide some idea of the frequency of extreme short-term rain rates and mesovortex collocation relative to other storm types using radar observations, and to create a case list of such collocations that can be used to examine the observed environmental characteristics associated with the events. It is hypothesized that extreme, hourly rainfall accumulations are collocated with meso-γ-scale rotation a majority of the time, which, in turn, provides evidence that the enhancement of rain rates by the dynamical effects of rotation outlined in NS18 are common in extreme, short-term rainfall scenarios.

---

[3] During tornado threats, it is recommend that you retreat to the lowest, central room of a sturdy building. However, for flash flooding scenarios, it is recommend that you retreat to higher ground.

Section 2 will present a few notable event examples, section 3 will present the methodology used, section 4 will present the results of the analysis, section 5 will present a discussion of the results, and section 6 and summary of the conclusions.

2. Representative event examples

Outside of the event discussed in detail in NS18 a few prominent events associated with intense one hour precipitation accumulations over 75 mm and attendant rotation on various scales are briefly discussed in this section. Additionally, an example of a case without the presence of rotation is presented.

On 21 June 2013 a storm with supercellular characteristics moved through southeastern North Dakota (Figs. 2a,b) and was responsible for producing two tornado and flash flood local storm reports (LSRs; IEM 2017) near Valley City, North Dakota. No flash flood warnings were issued for this storm; however, the temporal and spatial offsets between the tornado and flash flood LSRs still qualify this as a TORFF event (Nielsen et al. 2015), as do the next two events mentioned in this section. The 0055 UTC METAR observation at the Barnes County Municipal Airport (KBAC, denoted by black and orange markers in Figs. 2a and 2b, respectively) reported a one hour rainfall accumulation of 141.2 mm, while the maximum Stage-IV observation over that same period was 52.5 mm. The report location was nearly collocated with the rotation associated with the storm's mesocyclone (Fig. 2b), during this period of intense precipitation. The Bismarck, North Dakota, sounding valid 0000 UTC 21 June 2013 (Fig. 3a), the closest observed sounding to the event location (i.e., located west of the event location), contained $\sim$10 m s^{-1} of 0–1 km shear,[4] $\sim$30 m s^{-1} of 0–6 km shear, and a significant amount of CAPE (Fig. 3a), with a straight hodograph. The Storm Prediction Center's (SPC) Mesoscale Analysis (MA) archive showed 0–1 km shear values and lower 0–6 km shear values increasing toward the event location from Bismarck (Table 1). Further, the MA's depicted low-level storm relative helicity (SRH) values that easily were capable of supporting rotation (Table 1), with 0–1 km SRH values of $\sim$200 m^2 s^{-2} and 0–3 km values of $\sim$300 m^2 s^{-2}.

Another instance of extreme rainfall with attendant rotation was observed near Pensacola, Florida, and points northeast from $\sim$0130 to 0500 UTC on 30 April 2014 (Figs. 2c,d). An MCS with strong embedded

rotation (Fig. 2d) moved northeast during this period with its path tracing the approximate locations of the METAR observations (i.e., region bracketed by the four stations marked in Figs. 2c and 2d). One hour accumulations of 144.3, 84.8, 77.9, and 78.9 mm were observed at Pensacola International Airport (KPNS), Naval Air Station Whiting Field-South (KNDZ), Bob Sikes Airport (KCEW), and Duke Field (KEGI), Florida, respectively. The Stage-IV analysis recorded one hour estimates of 165 and 140.1 mm concurrent with the above METAR observations of the event. Further, throughout the day on 30 April the National Weather Service (NWS) forecast offices in Mobile, Alabama, and Tallahassee, Florida, issued twenty flash flood and thirteen tornado warnings (with many LSRs archived for both hazards; IEM 2017). Similarly to the previous case, the Tallahassee, Florida, sounding valid 0000 UTC 30 April 2014 contained $\sim$12 m s^{-1} of 0–1 km shear and a stable inversion (Fig. 3b), with similar values of 0–6 km shear. The shear metrics from the SPC MA show the impact of the event being farther west toward the synoptic forcing with 0–1 km shear approximated at $\sim$15 m s^{-1} and 0–6 km shear at $\sim$25 m s^{-1}. The low-level curvature seen in the hodograph (Fig. 3b) was also magnified farther west leading to, as in the previous case, low-level SRH values (e.g., $\sim$200 m^2 s^{-2} over 0–1 km) capable of supporting rotation (Table 1).

A third event occurred on 18 April 2016 in Houston, Texas. A mesoscale vortex embedded in a squall line moved through the area throughout the day (Figs. 2g,h) and produced significant flash flooding throughout the area. George Bush Intercontinental Airport (KIAH) recorded hourly accumulations of 98.6 and 81.0 mm during this event as the mesoscale vortex passed just to its north (Figs. 2g,h), while the maximum hourly Stage-IV accumulation during the same period was 113.8 mm. The Houston/Galveston NWS office issued 21 flash flood and 5 tornado warnings during this event (IEM 2017). Houston, Texas, is in a operational upper-air observation void (Benoit et al. 2018), with the closest remotely representative sounding located in Lake Charles, Louisiana (Fig. 3c). While the thermodynamic profile of this sounding is contaminated by convection and temporally incorrect, the hodograph shape, intense low-level shear, and more marginal deep-layer shear are consistent with the expectations from larger-scale, preconvective analyses. Given this, the SPC MA preconvective values had $\sim$15 m s^{-1} of 0–1 km and $\sim$20 m s^{-1} of 0–6 km shear present over the region (Table 1). This, due to the hodograph curvature in low levels, led to similar low-level SRH values as the previous two events. Further, the SRH values in these three events fall in the range of the MED_SHEAR and CONTROL cases in

---

[4] Throughout this section and the rest of the paper, the 0–1 km shear nomenclature will refer to the 0–1 km bulk wind difference, and the units will reflect such.
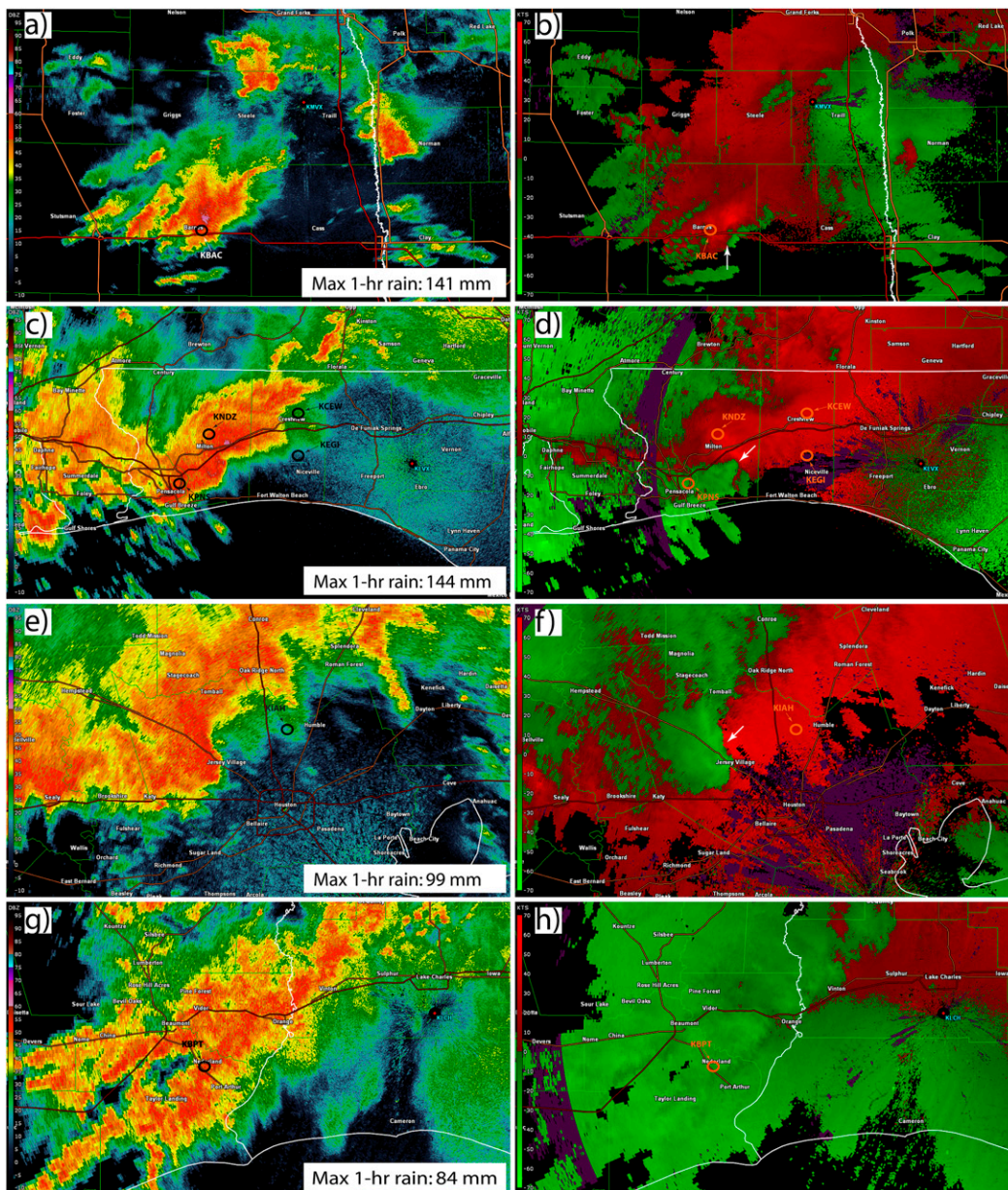
FIG. 2. (left) Radar reflectivity and (right) base velocity for three cases of 75 mm METAR rainfall accumulations with attendant mesoscale rotation. (left) Black and (right) orange dots represent location of METAR rainfall observations during the events. White arrows denote the locations of the attendant rotation. Images valid at (a),(b) 0021 UTC 21 Jun 2013 from Grand Forks, ND (KMVX), radar; (c),(d) 0222 UTC 30 Apr 2014 from Pensacola, FL (KEVX), radar; (e),(f) 0817 UTC 18 Apr 2016 from Houston/Galveston, TX (KHGX), radar; and (g),(h) 1210 UTC 18 Jul 2014 from the Lake Charles, LA (KLCH), radar. Individual METAR stations are labeled on the radar reflectivity plots for each case. Maximum one hour rainfall observations from local METAR or mesonet networks are labeled for each case (left column).

NS18, where the rotation induced dynamical accelerations that increased the resulting precipitation. In summary, these three events all had intense hourly rainfall rates observed in association with near collocated, mesoscale rotation in environments of 0–1 km shear and low-level helicity values that support the development of rotation.

A fourth event that did not have collocated rotation occurred in the morning hours of 18 July 2014 near Beaumont and Port Arthur, Texas (Figs. 2g,h). A developing surface low pressure system associated with a late summer long-wave trough and fairly robust upper-level forcing for ascent led to the development of an
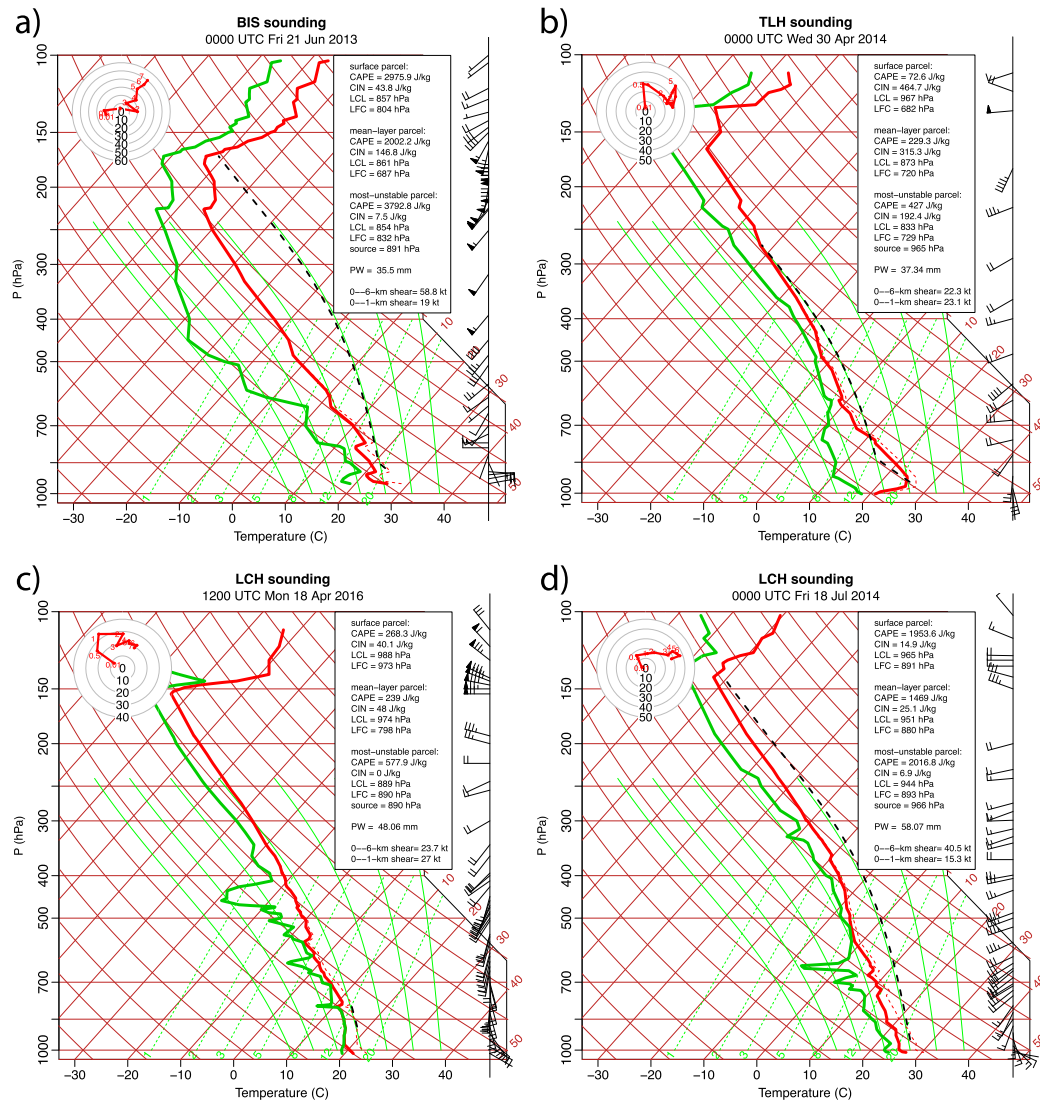
FIG. 3. Observed soundings valid at (a) 0000 UTC 21 Jun 2013 from Bismarck, ND, (b) 0000 UTC 30 Apr 2014 from Tallahassee, FL, (c) 1200 UTC 18 Apr 2016 from Lake Charles, LA, and (d) 0000 UTC 18 Jul 2014 from Lake Charles, LA. Dashed black line in each sounding represents the temperature of a lifted parcel with the maximum equivalent potential temperature θ_e, using the virtual temperature correction. Dashed red line in each sounding represents the virtual temperature correction to the temperature profile.

MCS that initiated north of Houston, Texas, near 0300 UTC that same day (not shown). This, combined with precipitable water values just under 60 mm (Fig. 3d), led to the development of intense, back building convection by 1000 UTC 18 July in the Beaumont/Port Arthur area (Figs. 2g,h). The 1253 UTC METAR observation from Jack Brooks Regional Airport (KBPT) recorded an hourly accumulation of 83.6 mm, compared to a maximum Stage-IV accumulation over the same period of 81.4 mm. Flash flood warnings were issued for the region by the Lake Charles NWS office beginning at 1223 UTC, and reports of flooding continued in the area until

approximately 1400 UTC (IEM 2017). The 0000 UTC preconvective sounding from Lake Charles, Louisiana, contained ~8 m s^{-1} of 0–1 km shear (Fig. 3d) and veering in the low-level wind profile. As the night progressed and the low-level jet was established, 0–1 km shear values increased to ~12.5 m s^{-1}, and 0–1 km SRH values approached 100 m^2 s^{-2} (Table 1). The environmental SRH values seen in this case are similar to the LOW_SHEAR case in NS18, which generated only short-lived, transient rotating features that produced little in the way of rotationally induced dynamical accelerations and precipitation enhancement. Unlike the

TABLE 1. Approximate preconvective kinematic values for each event as estimated by the Storm Prediction Center's Mesoscale Analysis image archive (SPC 2017). Listed kinematic values are valid as close as possible to the start of the period over which the identified extreme precipitation observation is valid and may differ compared to soundings in Fig. 3.

Event	0–1 km shear	0–6 km shear	0–1 km SRH	0–3 km SRH
North Dakota	$\sim$15 m s^{-1}	$\sim$20 m s^{-1}	$\sim$200 m^2 s^{-2}	$\sim$300 m^2 s^{-2}
Florida	$\sim$20 m s^{-1}	$\sim$25 m s^{-1}	$\sim$200 m^2 s^{-2}	$\sim$300 m^2 s^{-2}
Texas	$\sim$15 m s^{-1}	$\sim$20 m s^{-1}	$\sim$175 m^2 s^{-2}	$\sim$300 m^2 s^{-2}
Louisiana	$\sim$12.5 m s^{-1}	$<$15 m s^{-1}	$\sim$100 m^2 s^{-2}	$\sim$150 m^2 s^{-2}

previous three cases present in this section, the extreme hourly rainfall was not associated with attendant rotation, but rather a narrow region of intense back building convection (Figs. 2g,h; Schumacher and Johnson 2005).

3. Methods

To provide an idea of the frequency of extreme rain rate and mesovortex collocation using radar observations, hourly precipitation accumulation data were obtained spanning 2013–17 for rain gauges and 2013–15 for gridded multisensor precipitation products. The rain gauge dataset comprises METAR observations from across the United States acquired from the Iowa Environmental Mesonet (IEM 2018) and filtered to retain hourly accumulations greater than or equal to 75 mm. Additionally, hourly accumulations greater than or equal to 100 mm were also obtained from the National Center for Atmospheric Research of the NCEP Stage-IV gridded precipitation analysis (Lin and Mitchell 2005) between 2013 and 2015, which is a multisensor approach using both rain gauge– and radar-based QPE. The specific rainfall accumulation thresholds mentioned above (i.e., hourly accumulations of 75 and 100 mm for the METAR data and Stage-IV data, respectively) were applied across the contiguous United States (CONUS) to represent events that could be considered in the realm of 25–50-yr-average recurrence intervals (ARI) at the one hour accumulation threshold for the majority of CONUS (Stevenson and Schumacher 2014; Herman and Schumacher 2018b). While these hourly accumulations are not as extreme along the U.S. Gulf Coast and the southeastern part of the country (i.e., between 10- and 25-yr ARIs for hourly accumulations), these thresholds were still chosen to ensure an adequate sample size for analysis. Additionally, a rainfall rate of 75 to 100 mm h^{-1} sustained over an hour would likely lead to flooding of some magnitude, especially in urban areas (e.g., Smith et al. 2001, 2013), since surface runoff is largely controlled by rain rate (e.g., Woolhiser and Goodrich 1988; Beven 2012) and has been shown to increase proportionally to the

amount of built urban environment in the affected area (e.g., Gill et al. 2007).

It should also be noted that the list created by this method is by no means comprehensive nor are the measured values from the METAR observations (e.g., Legates and Deliberty 1993; Yang et al. 1998) or Stage-IV (e.g., Nelson et al. 2016) without errors. Additionally, given the increased spatial sampling associated with the remote sensing–based Stage-IV product compared to the sparse METAR gauge network, an attempt to maintain a similar relative exceedance frequency between the products was undertaken by increasing the filtering threshold to 100 mm h^{-1} in the Stage-IV dataset, compared to 75 mm h^{-1} in the METAR dataset. This also helps to make the number of points tractable for manual analysis. Similarly, the period over which the Stage-IV data were examined is shorter (i.e., 2013–15), compared to the METAR (i.e., 2013–17) dataset, due to the significant increase in data points per year in the spatially continuous Stage-IV product over the spatial discrete rain gauge data. Examining a similar temporal range of Stage-IV data would have made the manual analysis described below unfeasible. These temporal and accumulation threshold choices created a dataset that contains a sufficient number of events for analysis.

The gauge and gridded rainfall observations were then manually culled by regional radar analysis to filter out snowfall events, spurious accumulations/data in the Stage-IV analysis (e.g., Nelson et al. 2016; Herman and Schumacher 2016), and to remove rain gauge observations that were potentially reporting false data (e.g., no precipitation was visible on radar). Care was also taken to remove entries in the METAR data if the precipitation had ended and the gauge was still reporting continued rainfall. In the instance that multiple sub-hourly (i.e., special) observations, from the same gauge were present, the highest accumulation was recorded. Local radar data including equivalent reflectivity, differential reflectivity, and radial velocity, were obtained for the remaining points for the hour over which the observation was valid from the Unidata AWS Level II Radar Archive (Unidata 2018). These local radar data were then used to subjectively identify whether
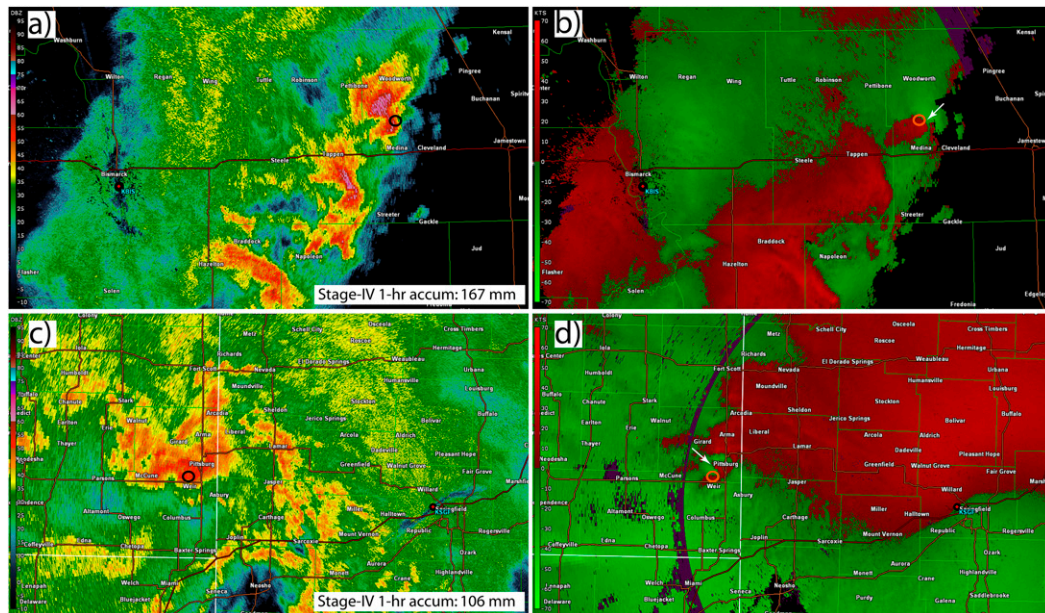
FIG. 4. (a),(c) Equivalent reflectivity (Z_H) and (b),(d) radial velocity from the (a),(b) Bismarck, ND (KBIS), and (c),(d) Springfield, MO (KSGF), NEXRAD radars valid at 0219 UTC 19 May 2013 and 0414 UTC 30 Jul 2013, respectively. Black and orange open circles in the reflectivity and velocity, respectively, denote location of extreme, short-term hourly rainfall accumulation over 100 mm from the Stage-IV analysis during which the radar images are valid. White arrows denote the locations of the subjectively identified rotation.

meso-γ-scale rotation, from either supercell or mesovortex like structures, was collocated with the identified points of extreme hourly rainfall accumulations at any time over the hour the precipitation accumulation was valid. An example of this process is presented for two points in Figs. 4a–d. The black and orange circular markers in the reflectivity and radial velocity fields, respectively, represent the location of a Stage-IV accumulation of over 100 mm in an hour. Examining the radar data for the period over which the observation was valid, meso-γ-scale rotation is identifiable and collocated with the Stage-IV point at some time in that hour, as shown for each case in Figs. 4a,b and Figs. 4c,d, respectively. Thus, these two points were subjectively identified as being associated with rotation because meso-γ-scale rotation was identifiable in the radar radial velocity in the convection at the location of the observation during the time in which the accumulation was measured.

Larger-scale rotation associated with mesoscale convective vortex (MCV) like structures (e.g., meso-β-scale or larger rotation) was not identified as rotation, as the rotational induced dynamics discussed in NS18 and in the introduction are likely not applicable for such features (e.g., see example rotation rates in: James and Johnson 2010). A subjective method was used as part of this analysis, since the focus is on rotation of various scales and strengths and that detection algorithms still remain subjective as to the exact parameters chosen

(e.g., Jones et al. 2004). Additionally, objective methods, such as azimuthal shear–based products, can lead to spurious detections in regions of strong deformation (e.g., gust fronts and other boundaries, Smith et al. 2016), false returns (e.g., ground clutter), and are sensitive to how the velocity data are dealiased. If any extreme rainfall observation was not associated with rotation or it was unclear for any reason, the point was classified as not being associated with rotation.

Initially, the resulting list of points of extreme hourly rainfall accumulations for the METAR and Stage-IV datasets were clustered into events, separately, using a density-based algorithm for spatial datasets with noise (DBScan; Ester et al. 1996) as implemented using the Scikit-learn (Pedregosa et al. 2011) Python programming library. This was done to avoid introducing biases in event identification and serve as a point of comparison within the datasets, since each dataset spans a different time period and is based upon a different precipitation accumulation threshold. Then, the clustering was redone entirely using both the METAR and Stage-IV observations combine to create a master list of events (see online supplement). Each event cluster was marked as a rotation event if at least one of the extreme hourly rainfall accumulations within the cluster was previously subjectively identified as being associated with rotation. If no observations within a cluster were associated with rotation, it was deemed to be a

nonrotation event. The resulting event clusters based upon both observational datasets were used to create event centered composites and parameter distributions from the Rapid Refresh (RAP; Benjamin et al. 2016) analysis to evaluate the environmental characteristics of extreme rainfall events with collocated rotation (i.e., rotation events) compared to those that did not (i.e., nonrotation events). Select native RAP model variables and derived variables were calculated and saved for the 260 km (i.e., 20 RAP grid points) in each primary direction from the individual event center. The resulting data for each event was then equally weighted to create event centered composites. The composites were made from the event clusters with all the south Florida, tropical cyclone (TC), and those west of the U.S. Continental Divide removed from both the rotation and nonrotation datasets. The weakly forced Florida cases were removed to avoid diluting the composites with weak synoptic signals from convective spin ups that are dominated by sea-breeze interactions that are likely not resolved well in the RAP. The cases located in the western United States were removed to exclude events that could be heavily influenced by orographic effects (e.g., Doswell et al. 1998). Similarly, the tropical cyclone cases were removed since the system wide kinematics and dynamics are quite different compared to continental convection (e.g., Baker et al. 2009; Morin and Parker 2011; Edwards et al. 2012). However, this does not lessen the importance of TCs in producing extreme short-term rainfall accumulations. Furthermore, 19 cases where radar data did not allow a conclusive subjective interpretation of whether rotation was present were not included in the composite analysis. However, these cases are still included in the general statistics as nonrotation cases.

Last, the diurnal, seasonal, and maximum accumulation distributions of the rotation and nonrotation events will be examined for the cases that are included in the composite analysis. The diurnal distribution was examined from a mean event UTC start time as well as relative to sunset. Information about the number of rainfall observations in each event and the event occurrence relative to sunset/sunrise were retained. The start time, date, latitude, and longitude of each individual rainfall observation in each event cluster was then used to calculate the local sunset and sunrise time for each rainfall observation using the Python programming language PyEphem library (Rhodes 2011). Each individual observation start time was then converted to a sunset and sunrise relative framework. This sunset/sunrise information for each rainfall observation within a specific event were used to determine the event timeline relative to the nocturnal evening transition (ET; Defined in this study as the two hour period prior and following local

sunset; Acevedo and Fitzjarrald 2001; Bonin et al. 2013; Anderson-Frey et al. 2016), which is characterized by continued relatively large MLCAPE, increasing 0–1 and 0–6 km SRH, and lowering LCL heights, which leads to an overall increase in the potential for rotation. The event clusters are discriminated into those that produce extreme, short-term rainfall observations from the afternoon past the end of the ET period (hereafter referred to as BOTH events), from events that produce their rainfall observations during or before the ET period (hereafter referred to as EARLY events), and from extreme rainfall events that occur exclusively after the ET period (LATE events), as determined by the METAR and Stage-IV observations responsible for each individual extreme, short-term rainfall event cluster. The overall motivation is to examine if there is increased prevalence for rotation or nonrotation events to occur relative to the ET or nocturnal period.

4. Results

A total of 136 METAR and 732 Stage-IV points (see online supplemental material for location and timing of all points) of accumulation over 75 and 100 mm per hour, respectively, were collected between 2013 and 2017 (Figs. 5a,b). A total of 66 (48.5%) of the METAR and 337 (46.0%) of the Stage-IV observations were associated with rotation on the meso-γ-scale (Figs. 5c,d, Table 2). The spatial distribution of the points associated with these extreme rain rates follow the Gulf and Atlantic coastlines and extend into the central plains (Figs. 5a,b), which follows what one would expect a priori based upon the 10–50-yr, 1-h ARIs for the United States (Perica et al. 2018; Herman and Schumacher 2018b). The points associated with and without collocated rotation follow a similar pattern (Figs. 5c,d) throughout the United States, and are more focused on the coastlines than in the inland regions (Figs. 5c,d and 6b,c).

A total of 299 extreme rainfall events (see supplemental material for location and timing of all event clusters) result in the dataset, once the clustering analysis using both the METAR and Stage-IV observations was undertaken (Fig. 6a). The geographic distribution of the events, by design, is similar to the individual observations of extreme rainfall seen in Figs. 5a and 5b. Of the 299 events in the combined dataset, 125 (41.8%) were associated with mesoscale rotation (Fig. 6b). The events with (Fig. 6b) and without (Fig. 6c) rotation follow similar geographic patterns, with the importance of a moisture reservoir (e.g., the Gulf of Mexico) having clear importance in both subsets. The Stage-IV data by itself was clustered into 214 events, of which 82 (38.3%) of the events were associated with rotation. However,
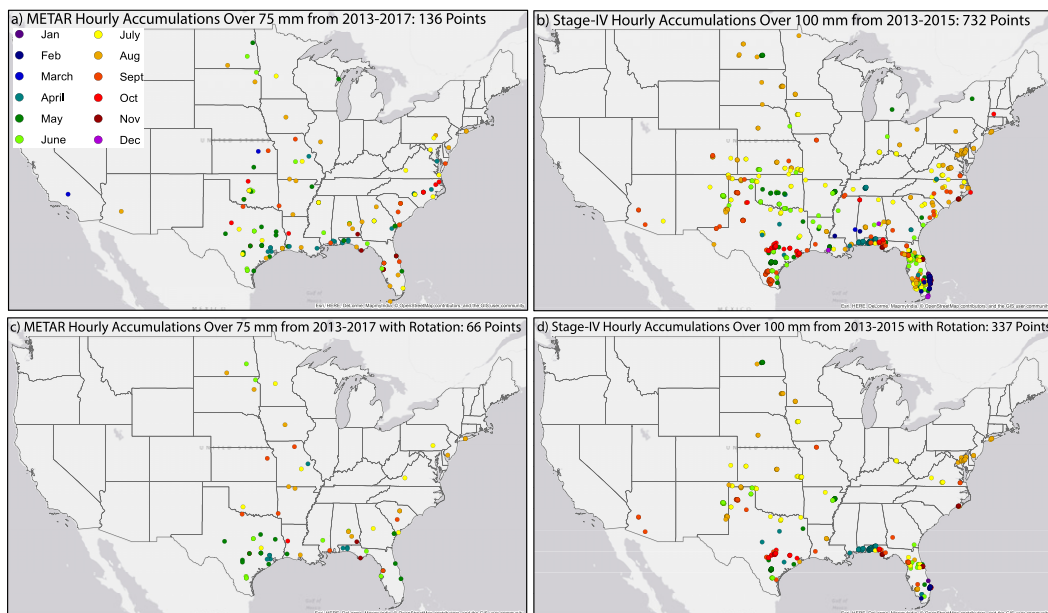
FIG. 5. Geographic distribution of (a),(c) METAR and (b),(d) Stage-IV hourly accumulations over 75 and 100 mm, respectively, (a),(b) not filtering for rotation and (b),(c) those observations only associated with rotation. A total of 66/136 points in the METAR and 337/732 of the Stage-IV dataset are associated with rotation.

the 82 events associated with rotation accounted for 468 of the 732 (63.9%) Stage-IV grid cells that exceeded $100 \, mm \, h^{-1}$, which implies that the rotation events might be, from an areal sense, more prevalent producers of extreme rainfall. The METAR data were clustered by itself into 111 total events, of which 54 (48.6%) were associated with rotation. Overall, depending on how the data are parsed, extreme precipitation events are associated with meso-γ-scale rotation ~40% of the time.

Seasonally, the events associated with rotation are more likely to occur in the late summer and are more confined to the warm season, compared to those without rotation (Fig. 7a). While the nonrotation events have a similar seasonal distribution to those with rotation, they occur more frequently in the winter months and early shoulder seasons (Fig. 7a). Further, the seasonal maximum of rotation events seems to appear slightly later in the year than the seasonal tornado maximum (e.g., Brooks et al. 2003). From a diurnal standpoint of the mean event start time, nonrotation event frequency was maximized in the early afternoon to evening hours (i.e., 1700–2200 UTC, Fig. 7b), while the events associated with rotation more commonly occur in the late evening to nocturnal hours (i.e., 0000–1400 UTC, Fig. 7b). There is overlap in the timing of peak frequency between the rotation and nonrotation events in the evening hours (i.e., 2100–2300 UTC, Fig. 7b), but the probability of rotation events increases, over the probability of non-rotation events, into the overnight hours.

The classification of the event clusters relative to the ET shows that majority of the extreme, short-term rainfall events that occur along the Florida peninsula are EARLY events (i.e., occur entirely before the end of the ET, Fig. 8a). This makes sense from what is known about the diurnal cycle of sea-breeze convection in the region (e.g., Byers and Rodebush 1948; Michaels et al. 1987). Nationally, EARLY events are responsible for just under 60% (Table 3) of all events and occur regularly throughout the geographic distribution of events (cf. Figs. 8a–c). LATE events (i.e., those that occur completely after the ET is complete) follow a similar geographic pattern to the EARLY events, apart from Florida and the Carolinas (Fig. 8c), and are responsible

TABLE 2. Statistical breakdown and number of points associated with or without rotation for the extreme rainfall observations from the METAR, Stage-IV datasets, and resulting event clusters utilized in this study.

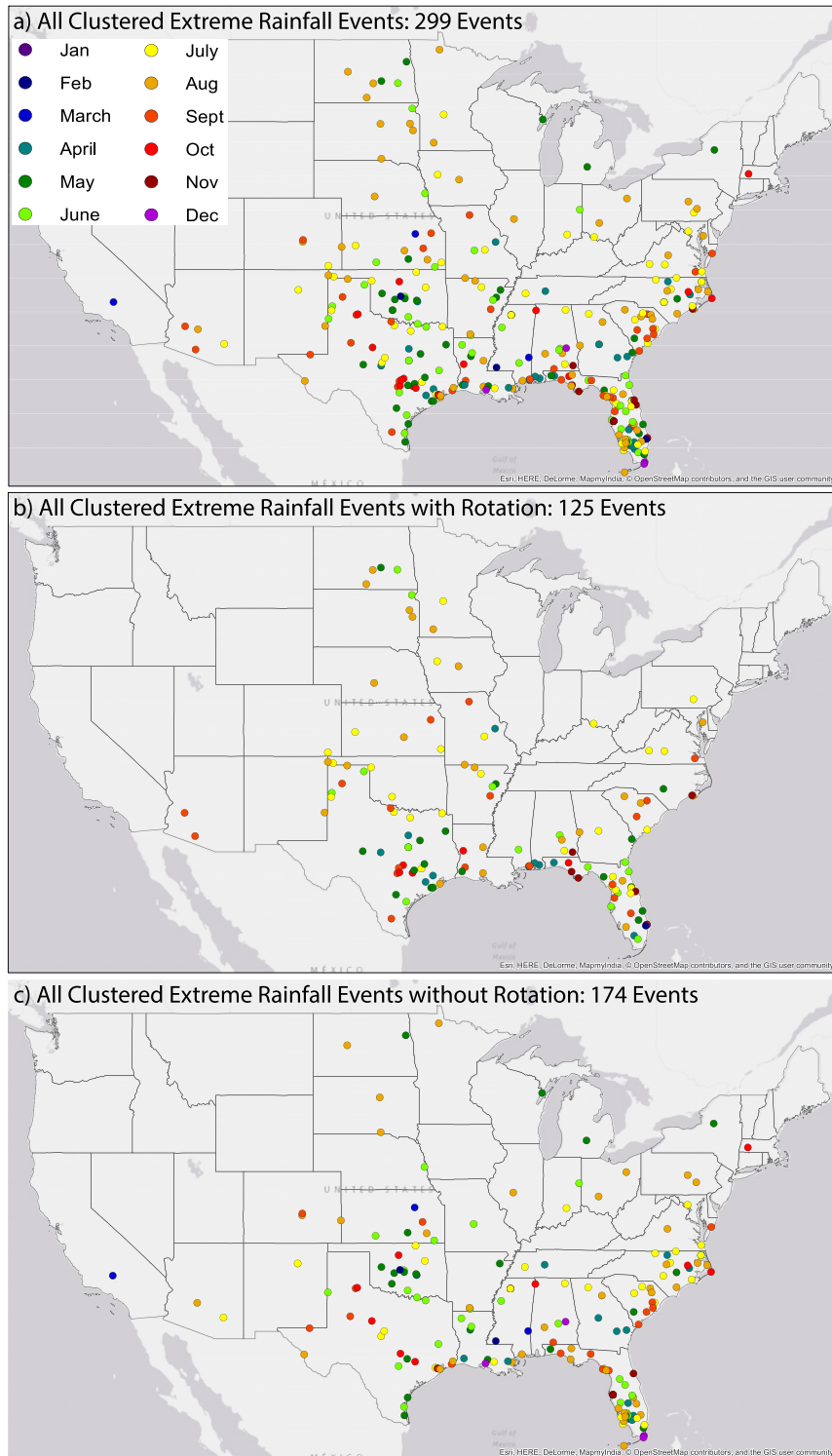| Dataset	Number of points/events	Points/events with subjectively identified rotation
METAR observations from 2013 to 2017 > $75 \, mm \, h^{-1}$	136	66 (48.5%)
Stage-IV observations from 2013 to 2015 > $100 \, mm \, h^{-1}$	732	337 (46.0%)
Event clusters	299	125 (41.8%)

FIG. 6. (a) Geographic depiction of all extreme rainfall event clusters created from both the METAR and Stage-IV datasets, (b) events that were subjectively identified with rotation, and (c) events not associated with rotation. Events color coded by month.
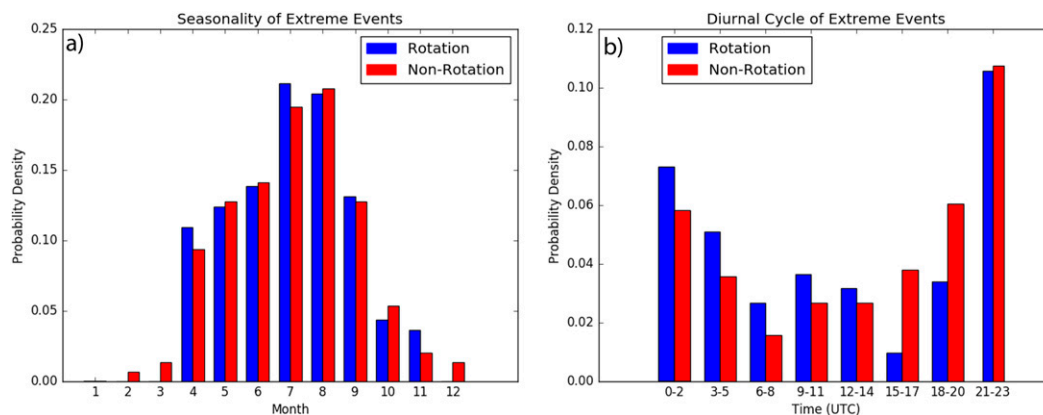
FIG. 7. (a) Seasonal and (b) diurnal distributions of the rotation (blue bars) and nonrotation (red bars) for the cases that were used to create the event centered composites in Figs. 11 and 12. Histograms are binned every (a) month and (b) every 3 h of local UTC time on the *x* axis vs, while probability density is on the *y* axis. Times in (b) reflect mean event start time.

for the next largest portion of extreme, short-term rainfall events (Table 3). BOTH events (i.e., events that produce observations of extreme, short-term rainfall before and after the ET) are relatively rare in the overall distribution, making up just under 10% of the event total (Table 3). They also occur primarily in the southeastern quadrant of the CONUS (Fig. 8b). Rotation events are associated with a higher percentage of LATE (16%) and BOTH (36.8%) events, compared to nonrotation events (4.0% BOTH and 29.9% LATE, Table 3). This follows the results of the mean event time distribution, discussed in above (Fig. 7b), showing the increased propensity for rotation events to be nocturnal. If the Florida peninsula cases are removed from each subset (as done in the composite analysis below), the majority of the rotation events are LATE, while the majority of the nonrotation events are EARLY (not shown). Additionally, the inland rotation events (Fig. 8) generally have more of nocturnal component to them (i.e., BOTH or LATE events), compared to the inland nonrotation events (Fig. 8).

Cases associated with coincident rotation tended to produce higher hourly accumulations that those without any rotation present (Fig. 9),[5] when examining values over 100 mm. This is true for both the mean (i.e., 121.5 mm) and median (i.e., 116.5 mm) of the cases

where rotation is present, compared to the cases where rotation is not present (i.e., mean of 114.5 mm and median of 110.0 mm, Fig. 9).

The RAP composites characterizing the mean environment at the start of the extreme rainfall for all of cases identified in this study are consistent with the ingredients that have been previously identified as needed for extreme precipitation (e.g., Doswell et al. 1996). The events tended to occur ahead of an upper-level trough (Figs. 10a,c,e) in the warm sector of an extratropical cyclone (Figs. 10b,d,e). The center of the events was located along a surface warm front/stationary boundary (Fig. 10b) near the nose of the lower-level jet (LLJ; Fig. 10d). The hint of a weak 500-hPa short wave (Fig. 10c), widespread 850-hPa warm air advection (Fig. 10g), and moderate levels of instability ($\sim$1500 J kg^{-1}; Fig. 10d) are also seen just upstream of the event center. A broad region of precipitable water (PWAT) over 45 mm ($\sim$1.75 in.; Fig. 10b) surrounds the event center, providing an ample supply of moisture. While the general flow aloft is weak and potentially points to slower storm motions, approximate 0–1 km shear[6] is over 7 m s^{-1} and RAP estimated 0–3 km storm relative helicity (SRH) approaches 150 m^2 s^{-2} (Figs. 10f,g). These values of 0–1 km shear and 0–3 km SRH, while less than expected for significant tornado environments, still fall within the ranges associated with rotating thunderstorms (e.g., Thompson et al. 2003; Craven et al. 2004; Thompson et al. 2012).

---

[5] This is true for the distribution of events where the maximum hourly accumulation is over 100 mm. This upper threshold was chosen to make the most clean comparison between the METAR- and Stage-IV-based events, since the 75 mm h^{-1} minimum was used originally for the METAR events and skews the distribution of both rotation and non-rotation events. However, there is still a more pronounced tale of higher accumulations in the rotation cases, compared to the non-rotation cases, when all clusters are used in the analysis.

---

[6] Since the RAP does not have native variables to calculate the 0–1 km wind shear, it was approximated as the bulk wind difference between the 10 m wind and mean 90–120-mb layer above ground wind.
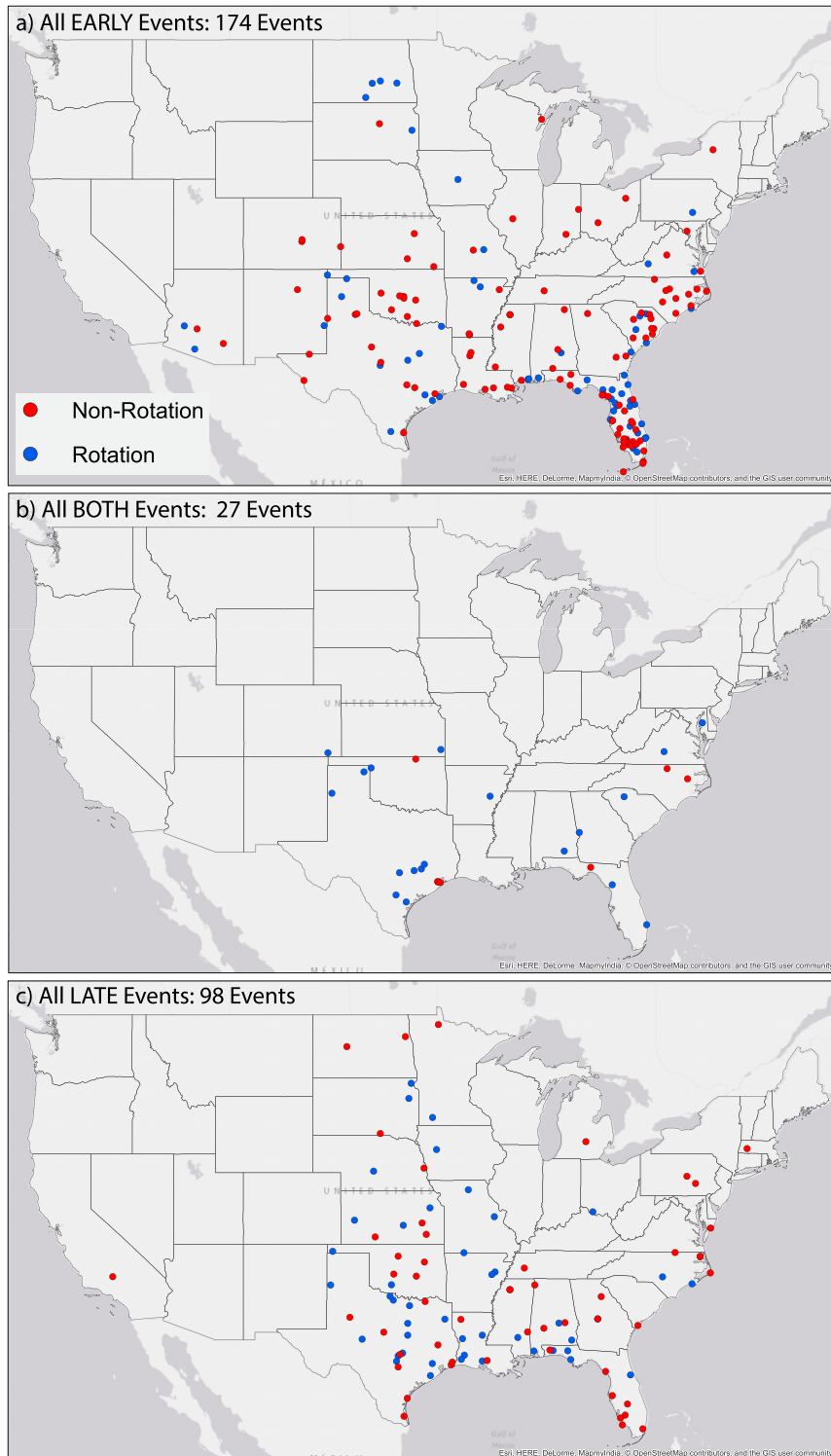
FIG. 8. Geographic depiction of all extreme rainfall event clusters created from both the METAR and Stage-IV datasets classified as (a) EARLY, (b) BOTH, and (c) LATE diurnal event classifications discussed in section 3. Events are color coded by the presence of rotation.

TABLE 3. Statistical breakdown of the master list of extreme, short-term rainfall event clusters relative to the evening transition.

Data Subset	EARLY	BOTH	LATE
All event clusters ($n = 299$)	174 (58.2%)	27 (9.0%)	98 (32.8%)
Events with rotation ($n = 125$, 41.8%)	59 (47.2%)	20 (16.0%)	46 (36.8%)
Events without rotation ($n = 174$, 58.2%)	115 (66.1%)	7 (4.0%)	52 (29.9%)

FIG. 9. As in Fig. 7, but for the distribution of 1-h rainfall accumulations (mm, x axis) for the rotation (blue bars) and nonrotation (red bars) binned every 10 mm. Mean and median of rotation cases are 121.5 and 116.5 mm, respectively. Mean and median of nonrotation cases are 114.5 and 110.0, respectively.

The composites for the both the rotation and nonrotation events show some subtle synoptic and mesoscale differences between the subsets, with the main differences seen in the low-level wind and moisture characteristics. The nonrotation cases are associated with slightly slower flow aloft (Figs. 11a,b) and slightly lower heights at the mid- to upper levels (Figs. 11a–d), but both composite subsets show a signal of a short wave embedded in the flow (Figs. 11c,d), which is denoted by a small region of cyclonic relative vorticity but no clear signal in the height or wind field. However, the short wave is slightly north of the event center in the nonrotation cases, as compared with being at or upstream of the event in the cases with rotation (Figs. 11c,d). At lower levels (i.e., 850 hPa) the heights are lower and the winds more southerly for the cases with rotation (Figs. 11e,f). A tighter 850-hPa temperature gradient, slightly higher 850-hPa temperature, and more gradient perpendicular 850-hPa flow also lead to increased warm air advection in the rotation cases relative to the cases without rotation (Figs. 11e–h).

On the meso-to-convective scale, more differences between the rotation and nonrotation cases appear in the composites. The rotation cases are located more in the warm sector at the surface (Figs. 12a,c), while the nonrotation cases are located along what appears to be a warm front/stationary boundary and closer to the surface low pressure center (Fig. 12b). An expected northwestern shift is seen in the circulation at 900 hPa, given the surface circulation, in the cases without rotation with the flow remaining relatively weak (Figs. 12b,d). There appears to be a stronger and more backed low-level jet at 900 hPa in the cases associated with rotation (Figs. 12c,d); however, both event subclasses appear to occur at the nose of the LLJ. The apparent increase in the speed of the LLJ in the rotation cases could be explained by the increased frequency of nocturnal rotation events relative to nonrotation events (Fig. 7b). Furthermore, the increase in the speed of the LLJ could also be partially attributable to more intense LLJs and the associated increased low-level vertical wind shear being more conducive to rotation.
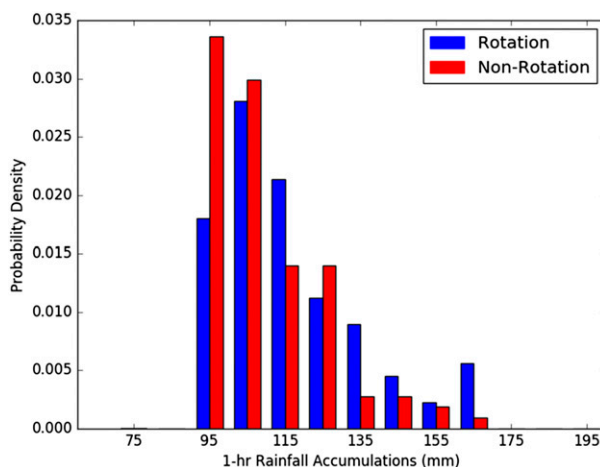
Both nonrotation and rotation case composites contain similar values of mixed-layer convective available potential energy (MLCAPE; Figs. 12c,d), despite the rotation cases being located more firmly in the warm sector relative to the nonrotation cases (located along the warm front). Precipitable water values are higher at event center in the warm sector in the rotation cases relative to the nonrotation cases (Figs. 12a,b). These rotation cases were associated with increased values of 0–3 km helicity, 0–1 km helicity, and approximate 0–1 km shear (Figs. 12e–h). Given the environmental conditions that are known to be conducive to rotation, this is not necessarily surprising.

Given the wide range of cases examined and the relatively small differences in the event center composites, the distributions of select fields were calculated as in Potvin et al. (2010) in the presumed storm inflow region to better determine the nature of the differences. Generally, the distributions between the rotation and nonrotation cases are very similar for the thermodynamic, moisture, and low-level kinematic variables (Fig. 13); however, there are a few instances where the the rotation cases tend to show more power in the upper half of the distribution of these parameters. This leads to the means of the rotation being statistically significantly higher[7] than those in the nonrotation cases for PWAT, 0–3 km storm relative helicity, 850-hPa temperature advection, and approximate 0–1 km shear. The broadening

---

[7] As calculated by a one-sided Z test at the 99.0% confidence level.

of the higher end of the distribution in the rotation events is most prominent in the PWAT (Fig. 13a) and approximate 0–1 km shear (Fig. 13e) distributions. In addition to the broadening in the upper half of the PWAT distribution in the rotation events, the nonrotation event distribution has values regularly occurring below the minimum in the rotation cases (i.e., below ~30 mm; Fig. 13a). While the increase in the upper portion (i.e., above $8 \, \mathrm{m \, s^{-1}}$) of the approximate 0–1 km shear distribution in the rotation cases is the largest among the low-level shear variables (Fig. 13e), similar, smaller increases in power are seen in the upper half of the RAP estimated 0–1 km (i.e., between 100 and $200 \, \mathrm{m^2 \, s^{-2}}$) and 0–3 km (i.e., between 200 and $600 \, \mathrm{m^2 \, s^{-2}}$) storm relative helicity distributions as well (Figs. 13c,d). The distribution of 850-hPa temperature advection is similar between the rotation and nonrotation cases, with the exception of a few outliers and an increased broadening near $0.5–1 \, \mathrm{K \, h^{-1}}$ in the rotation cases (Fig. 13b). In general, the distributions of the low-level kinematic values between the rotation and nonrotation events are similar; however, the low-level shear is more intense in the rotation cases.

5. Discussion

The surface and synoptic pattern for the nonrotation cases of extreme short-term rainfall is fairly consistent with the "frontal" archetype presented in Maddox et al. (1979). The ability of the surface boundary to repeatedly develop storms in the same area and the atmospheric mean flow to create a slow, boundary parallel storm motion leads to intense rainfall accumulations. On longer time scales, "training" events such these are well known flash flood and extreme rainfall producers (e.g., Doswell et al. 1996; Schumacher and Johnson 2005). However, on time scales examined in this study (i.e., hourly rainfall accumulations), the effects of storm motion/propagation are not as explicitly important, since in the vast majority of the cases it is raining intensely over the entire hour in order to yield the observed accumulations. This, in effect, removes the storm duration as a controlling factor on the extreme, short-term events examined in this study. However, the rain rate and all the processes that affect it, including rotation (NS18), clearly, still play an important role in these scenarios.

The presence of attendant rotation nearly half of the time when extreme hourly rainfall accumulations are observed supports recent studies that have identified storms that possess rotation on the meso-γ scale, most often supercells, as prevalent producers of extreme rainfall (e.g., Smith et al. 2001; Duda and Gallus 2010; Hitchens and Brooks 2013; Weijenborg et al. 2017; Smith et al. 2018), but falls short of the hypothesized

majority in this paper. The distribution of maximum event accumulations (Fig. 9) reinforces the idea that rotation events tend to produce higher hourly accumulations/rain rates then nonrotation events; however, known uncertainties exist surrounding the overall accuracy of both the datasets used in this analysis. Additionally, the 82 (38.3%) rotation events in the Stage-IV dataset that are associated with rotation produce 64% of the hourly gridded precipitation accumulations over 100 mm, which implies that the rotation events are more prevalent areal and/or persistent producers of extreme short-term rainfall. This latter point is also potentially supported by the increased percentage of BOTH events in the rotation subset (i.e., events that produce observations before and after the ET); however, the sample size of BOTH events is small in the dataset (~10% of total). These results not only support the general premise that rotational induced dynamical forcing on extreme rainfall is, at the very least, not necessarily prohibitive in producing extreme short-term rain rates, but also suggest that the presence of rotation could lead to the enhancement of the short-term rain rates, as discussed in NS18.

An attempt was undertaken to characterize the storm modes of the rotation and nonrotation cases identified in this paper. The storms themselves occurred across a very large variety of commonly classified meteorological modes, including MCSs, sub-MCS-scale convective clusters, scattered tropical/monsoonal/midlatitude convection, frontal convection, isolated supercells, supercells embedded within MCSs, and periods of upscale growth between discrete and organized convective modes. In general most of the cases, especially the ones associated with rotation, could be considered "messy." This is not necessarily surprising, given that the environments in all cases are supportive of convective development (Figs. 10–12), but made any classification scheme that accurately described the complexity of the various events offered limited value. However, most rotation events were associated with embedded rotating elements within a larger system that, at times, showed local enhancements in the reflectively field in the regions that were rotating (Figs. 2 and 4).

The overall composites (e.g., Fig. 10) give a baseline look into the bulk situations that are conducive for extreme, short-term rainfall, with the most interesting result, perhaps, that the maximum low-level vertical wind shear is approximately located over the expected inflow region for a rotating storm (Figs. 10f,h). Upon examining the results of the composite subsets, the synoptic-to-mesoscale conditions do not clearly distinguish between the rotation and nonrotation cases, partially because it is difficult to control for storm-scale differences in moisture and forcing for ascent. The composites in general
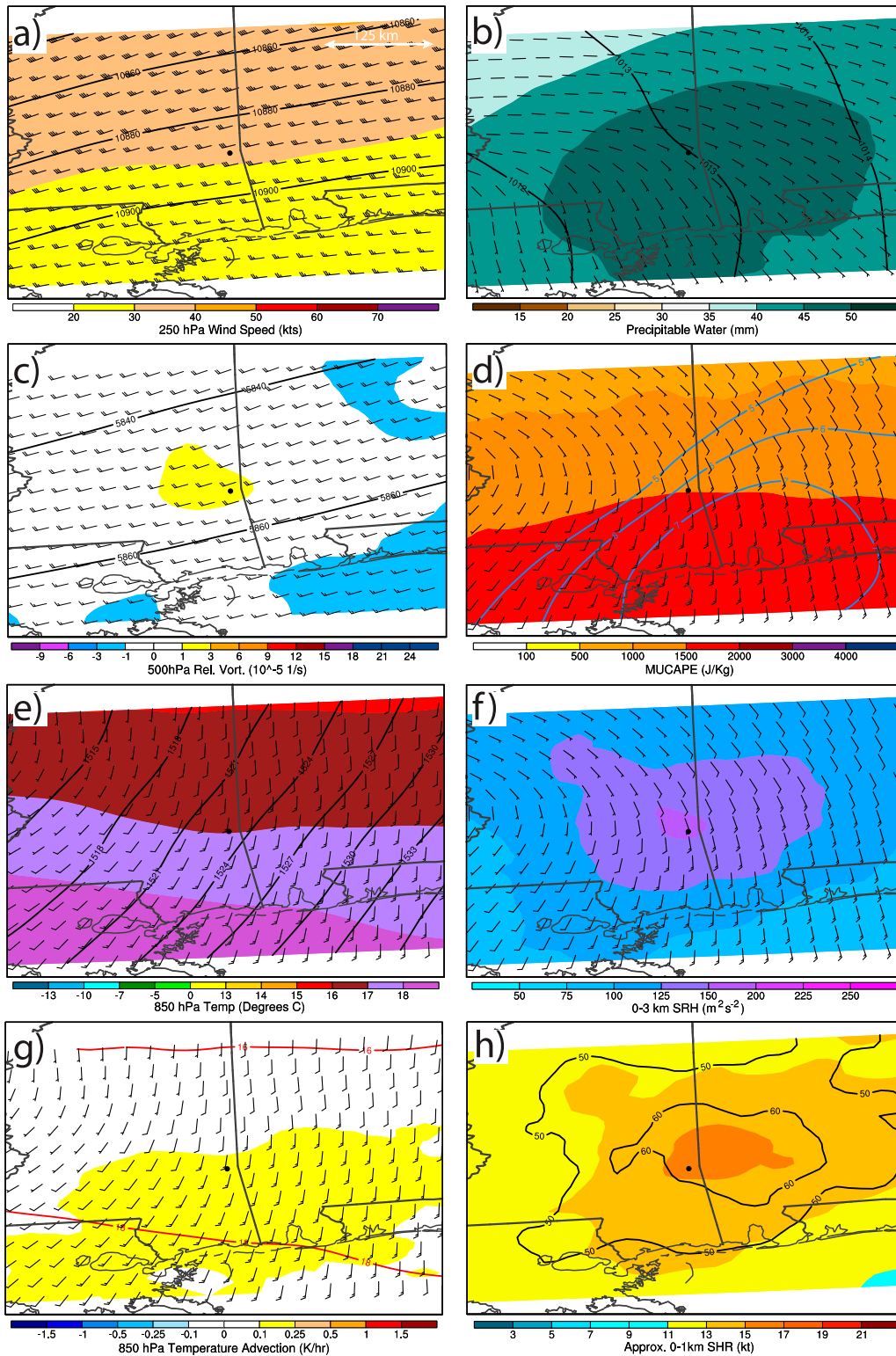
Fig. 10. Event centered composites for all the extreme precipitation events in this study. (a) 250-hPa heights (black contours, m), wind barbs (half barb = 5, full barb = 10, pennant = 50 kt, 1 kt = 0.5144 m s^{-1}), and 250-hPa isotachs (shaded, kt). (b) Mean sea level pressure (black contours, hPa), 10-m wind barbs, and precipitable water (shaded, mm). (c) 500-hPa heights (black contours, m), 500-hPa wind barbs, and 500-hPa relative vorticity (shaded,

point to stronger meso-to-synoptic-scale forcing (e.g., stronger 850-hPa warm-air advection) for ascent in the rotation composites (Figs. 11e–h). Additionally, higher PWAT in both magnitude and overall spatial extent is seen in the rotation cases compared to the nonrotation cases (Figs. 12a,b). These differences could explain why the rotation events appear to produce more intense and longer-lasting short-term extreme rainfall events (Fig. 9). However, there is no guarantee that the thermodynamically driven updrafts, alone, in the rotation cases are able to efficiently lift and utilize the additional moisture for precipitation production, especially, since both rotation and nonrotation cases have very similar amounts of instability (Figs. 12c,d) and that rotation cases have more potential to be occurring in the presence of nocturnal stabilization (Fig. 7b). These more pronounced ingredients for extreme rainfall in the rotation cases do add a compounding factor into the attribution of the exact environmental processes leading to these extreme short-term rain rates and the influence of rotation in these cases.

The increased presence of rotation events during the overnight hours (Fig. 7b) and number of rotation events that were classified as LATE or BOTH in the ET relative classification (Fig. 8, Table 3) potentially points to two important processes that are related to the impact that rotation can have on the storm system: nocturnal boundary layer stabilization and the enhancement of the low-level shear by the nocturnal low-level jet (LLJ), where the latter has been shown to have a positive impact on rotating storms (e.g., Markowski and Richardson 2014; Coffer and Parker 2015; Trapp et al. 2017). The overall increased low-level shear of the rotation cases (cf. Figs. 12e,g and Figs. 12f,h) and the signal of the LLJ in the rotation composites (Fig. 12c) hint at environments being more favorable for rotation and follow with the idea that any rotationally induced dynamical enhancement of the updrafts would likely occur in the lower levels of the storms. This is shown in the results of NS18 where the dynamic rotational enhancement of the updrafts occurred in the low levels as 0–1 km shear increased (see NS18's Fig. 15), which in turn enhanced the rainfall accumulations in the model simulations.

Given that similar environmental cues are seen in the composites as in NS18, it is not unreasonable to suspect that similar rotational enhancement mechanisms are active in at least some of the extreme rainfall cases with attendant rotation; however, the results are not directly conclusive.

While the effect of rotation on precipitation efficiency is not discussed in this manuscript and is very difficult to accomplish from a bulk sense, it remains an important question that authors plan to look at in specific cases moving forward. Further, the subjective radar analysis is only as good as the radar data that was examined. Data quality issues surely exist based upon distance from the radar, beam blockage, and attenuation, which all could affect the subjective identification of rotation. These issues, which are known to the authors, informed the decision to be as conservative as possible in the subjective rotation versus nonrotation sorting as discussed in the methods.

Overall, the authors feel that there are a few avenues moving forward that would be worth exploring to expand the climatology and potentially yield more conclusive results. One potential avenue would be to use a completely radar-based approach on shorter time scales, where identified regions of meso-γ-scale rotation are tracked and real-time, dual-pol radar rainfall estimates are used to evaluate precipitation rates for rotating regions. This approach, while limited by the various caveats associated with radar-based remote sensing, would allow for the creation of a more robust distribution of rainfall rates versus rotation strength and longevity. This could be also accomplished for various rainfall accumulations periods (i.e., 5-, 10-, 30-min, 1-h, etc). Furthermore, this would also allow the direct comparison, in cases of embedded rotation, of rain rates associated with nonrotation features within the same convective system. This would also allow for the convection to be subset on a region basis, which is likely important given the challenges with the events in Florida seen in this study. Additionally, the composite analysis undertaken in this manuscript was likely limited in both the temporal and spatial resolution of the underlying analysis, especially given the likely importance of mesoscale features in these events. Utilizing

←

$\times 10^{-5}\,\mathrm{s}^{-1}$). (d) 900-hPa isotachs (blue contours, $\mathrm{m\,s}^{-1}$), 900-hPa wind barbs, and MUCAPE (shaded, $\mathrm{J\,kg}^{-1}$). (e) 850-hPa heights (black contours, m), 850-hPa wind barbs, and 850-hPa temperature (shaded, °C). (f) 900-hPa wind barbs and 0–3 km storm relative helicity (shaded, $\mathrm{m^2\,s}^{-2}$). (g) 850-hPa temperature (red contours, °C), 850-hPa wind barbs, and 850-hPa temperature advection (shaded, $\mathrm{K\,h}^{-1}$). (h) 0–1 km storm relative helicity (black contours, $\mathrm{m^2\,s}^{-2}$) and approximate 0–1 km bulk wind difference (shaded, kt). It should be noted that all the composite figures shown in this manuscript (i.e., this figure and Figs. 11 and 12) are plotted with geographic map backgrounds, which are only there to represent scale and are not indicative of actual event locations (outside of the mean event center of each subset).
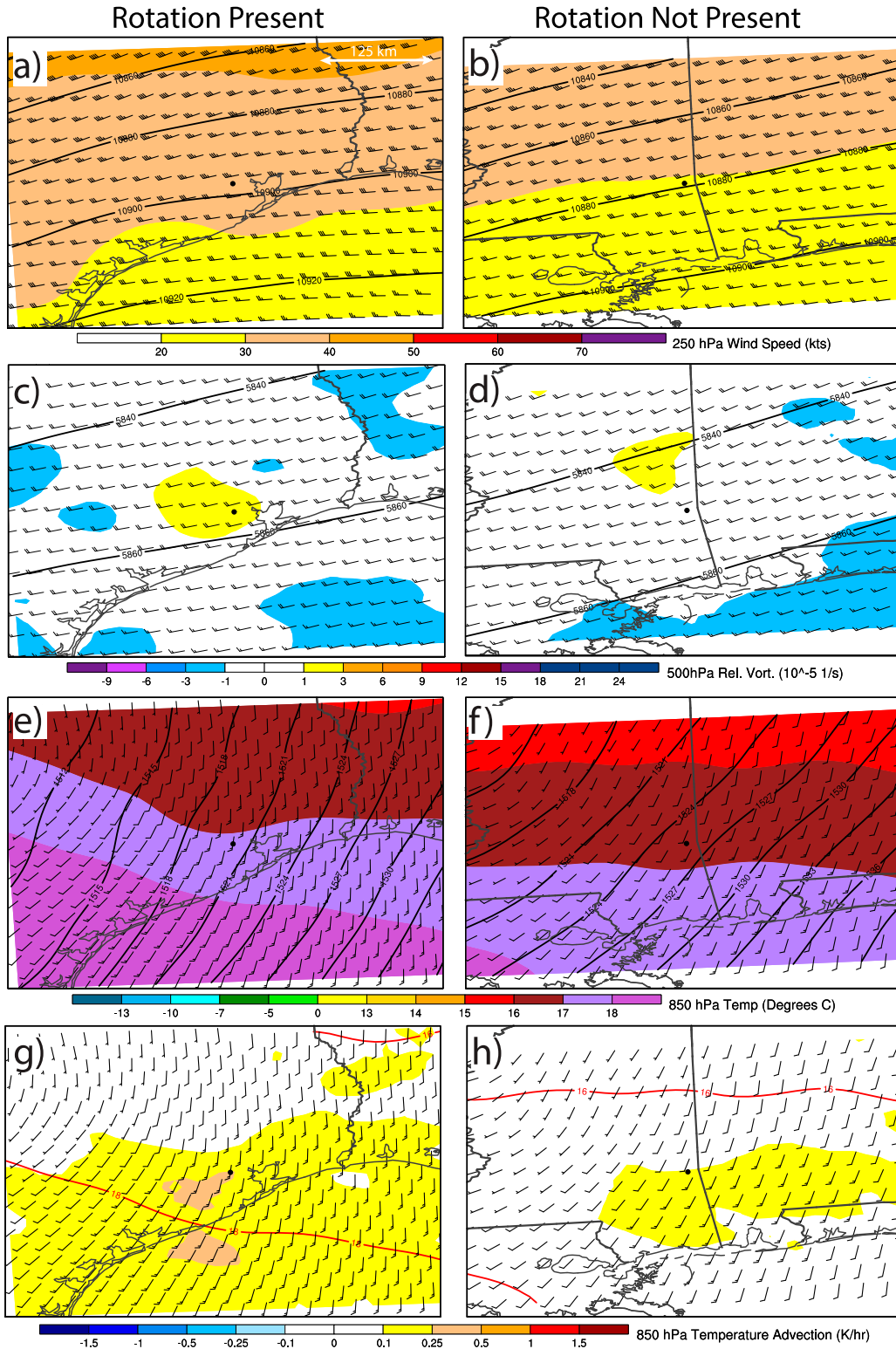
FIG. 11. (a),(b), (c),(d), (e),(f), (g),(h) As in (a),(c),(e),(g) of Fig. 10, respectively, for the (left) rotation and (right) nonrotation extreme precipitation events.
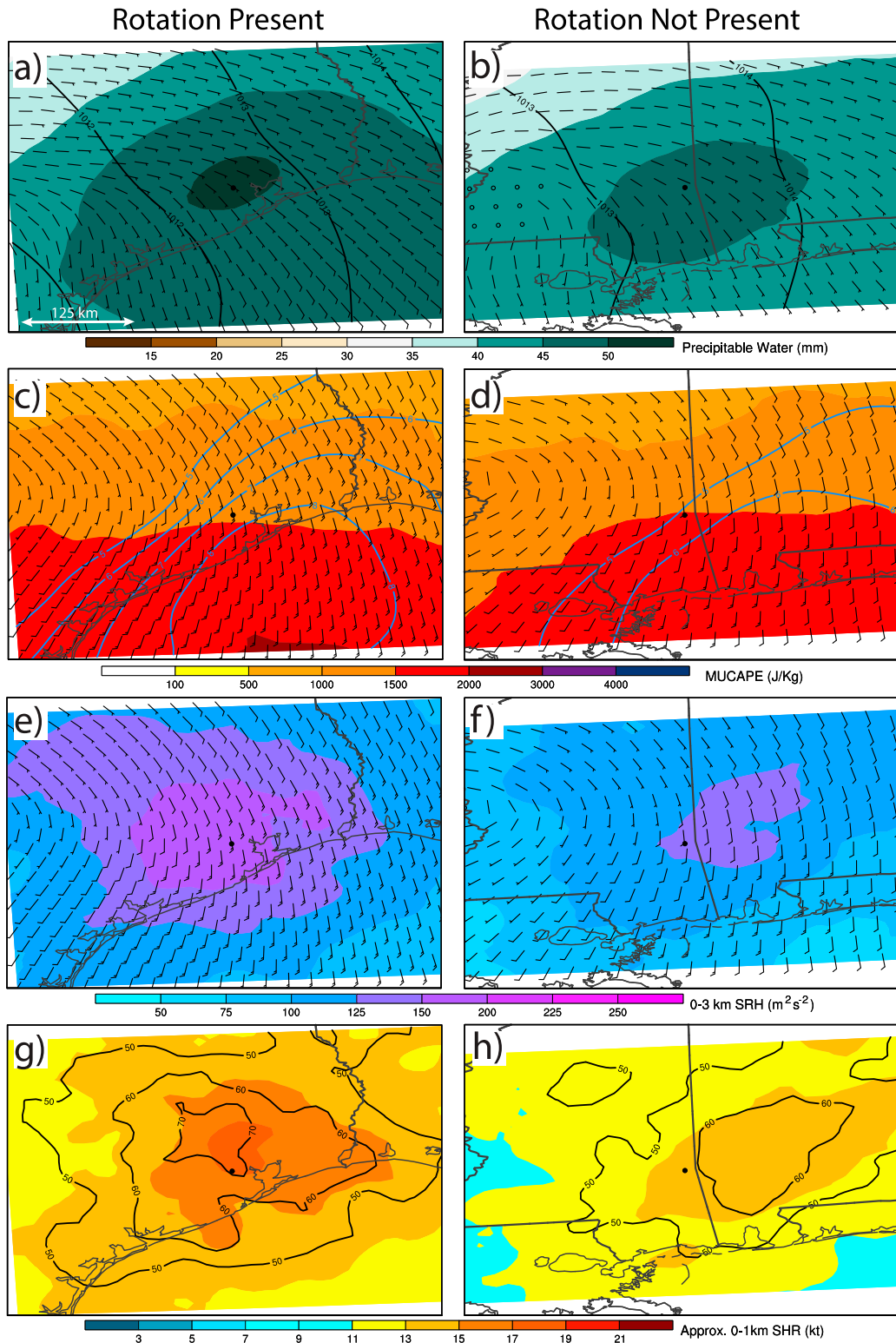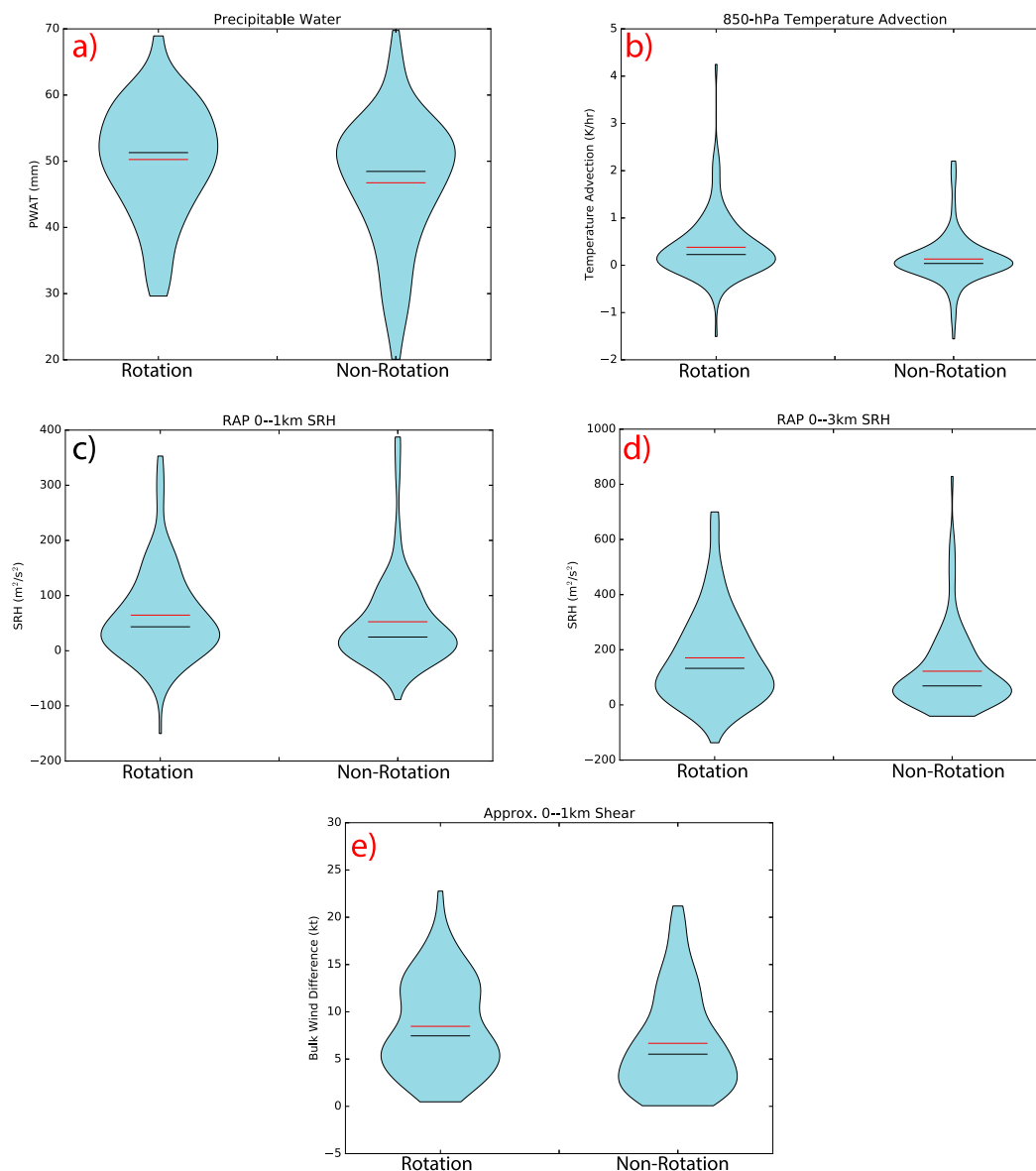
Rotation Present   Rotation Not Present

FIG. 12. (a),(b), (c),(d), (e),(f), (g),(h) As in (b),(d),(f),(h) of Fig. 10, respectively, for the (left) rotation and (right) nonrotation extreme precipitation events.

FIG. 13. Violin plots of (a) precipitable water (mm), (b) 850-hPa temperature advection $(K h^{-1})$, (c) RAP 0–1 km storm relative helicity $(SRH, m^2 s^{-2})$, (d) RAP 0–3 km storm relative helicity $(SRH, m^2 s^{-2})$, and (e) approximate 0–1 km shear/bulk wind difference in the presumed inflow region for the rotation and nonrotation events. Black lines denote the median and red lines the mean. Red panel labels in (a), (b), (d), and (e) denote that rotation means are statistically significantly higher than the nonrotation cases at the 99.0% confidence interval.

the analyses or 1-h forecasts from the High-Resolution Rapid Refresh (HRRR; Smith et al. 2008) would potentially allow for the inclusion of better resolved mesoscale features and the examination of storm-scale influence on the local environment.

6. Summary and conclusions

In this study, the frequency and environmental characteristics of extreme hourly rainfall accumulation events with attendant rotation was examined across the contiguous United States. METAR rain gauge observations and the Stage-IV gridded precipitation analysis during 2013–17 and 2013–15, respectively, were examined to produce a list of valid convectively driven extreme hourly rainfall accumulations. These points were then subjectively analyzed for the presence of collocated rotation during the hour the observation was valid. The resulting points were clustered into events, and event center composites created from the RAP to

investigate meteorological characteristics of both events with attendant rotation and those events without.

The results show that just under half of the subjectively identified individual observations associated with extreme hourly rainfall accumulations in the METAR and Stage-IV were associated with collocated rotation (see section 4 and Table 2). When clustered into events, 41.8% of the events were associated with meso-γ-scale rotation. The events with collocated rotation, similar to those without rotation, occurred along the Atlantic and Gulf coasts with points extending north into the Great Plains and lower Mississippi Valley, with both event types more common to the coastal regions and inland Texas (Figs. 5 and 6).

Seasonally, rotation events occurred more frequently in the warm season and are more likely in the mid to late summer. While nonrotation events share a similar distribution, they also occurred into the late winter months, unlike the rotation events (Fig. 7a). Rotation and non-rotation extreme precipitation events tend to peak with diurnal heating, but rotation events are more common in the late evening and overnight hours (Fig. 7b). Additionally, a larger portion of rotation event clusters tend to produce extreme, short-term rainfall throughout and after the ET (Fig. 8, Table 3). Rotation events tend to produce higher maximum hourly rainfall accumulations above 100 mm (Fig. 9). Slight, but potentially important, differences are also seen in the between the meteorological characteristics of each event subclass. Rotation events occurred more clearly in the warm sector and were associated with higher low-level shear, PWAT, 850-hPa warm air advection, and slightly weaker winds aloft (cf. left and right columns Figs. 11 and 12). Nonrotation events tended to occur along a surface boundary, such as a warm or stationary front, closer to the surface low pressure center with similar amounts of MUCAPE as rotation events (cf. left and right columns Figs. 11 and 12).

The results of this study agree with previous studies that highlight rotating storms as potentially underrepresented producers of extreme rainfall (e.g., Smith et al. 2001; Duda and Gallus 2010; Hitchens and Brooks 2013; Weijenborg et al. 2017) and that dynamically induced accelerations, especially those associated with rotation, can contribute, or at the very least are not always detrimental, to the production of extreme, short-term precipitation. It also provides observational support that the mechanism for rotational enhancement of rain rates presented in NS18 could be acting more frequently outside of the most extreme events and continues the discussion of a potentially common physical mechanism behind the occurrence of concurrent, collocated tornado flash flood events (Nielsen et al. 2015). Ongoing work will attempt to examine individual cases of extreme hourly rainfall accumulations with attendant rotation from a nonidealized, 3D modeling framework to examine more precisely how the presence of rotation directly or indirectly affects the development of precipitation from a microphysical standpoint.

REFERENCES

Acevedo, O. C., and D. R. Fitzjarrald, 2001: The early evening surface-layer transition: Temporal and spatial variability. *J. Atmos. Sci.*, **58**, 2650–2667, https://doi.org/10.1175/1520-0469(2001)058<2650:TEESLT>2.0.CO;2.

Anderson-Frey, A. K., Y. P. Richardson, A. R. Dean, R. L. Thompson, and B. T. Smith, 2016: Investigation of near-storm environments for tornado events and warnings. *Wea. Forecasting*, **31**, 1771–1790, https://doi.org/10.1175/WAF-D-16-0046.1.

Ashley, S. T., and W. S. Ashley, 2008: Flood fatalities in the United States. *J. Appl. Meteor. Climatol.*, **47**, 805–818, https://doi.org/10.1175/2007JAMC1611.1.

Baker, A. K., M. D. Parker, and M. D. Eastin, 2009: Environmental ingredients for supercells and tornadoes within Hurricane Ivan. *Wea. Forecasting*, **24**, 223–244, https://doi.org/10.1175/2008WAF2222146.1.

Benjamin, S. G., and Coauthors, 2016: A North American hourly assimilation and model forecast cycle: The Rapid Refresh. *Mon. Wea. Rev.*, **144**, 1669–1694, https://doi.org/10.1175/MWR-D-15-0242.1.

Benoit, M. D., C. J. Nowotarski, D. T. Conlee, and L. Wood, 2018: Impacts of a university-led, on-demand sounding program on human and numerical weather prediction model forecasts in an upper-air observation hole. *J. Operational Meteor.*, **6**, 74–86, https://doi.org/10.15191/nwajom.2018.0607.

Beven, K. J., 2012: *Rainfall-Runoff Modelling: The Primer*. 2nd ed. John Wiley & Sons, 488 pp.

Bonin, T., P. Chilson, B. Zielke, and E. Fedorovich, 2013: Observations of the early evening boundary-layer transition using a small unmanned aerial system. *Bound.-Layer Meteor.*, **146**, 119–132, https://doi.org/10.1007/s10546-012-9760-3.

Brooks, H. E., C. A. Doswell III, and M. P. Kay, 2003: Climatological estimates of local daily tornado probability for the United States. *Wea. Forecasting*, **18**, 626–640, https://doi.org/10.1175/1520-0434(2003)018<0626:CEOLDT>2.0.CO;2.

Browning, K. A., 1977: The structure and mechanism of hailstorms. *Hail: A Review of Hail Science and Hail Suppression, Meteor. Monogr.*, No. 38, 1–43, https://doi.org/10.1007/978-1-935704-30-0_1.

Bunkers, M. J., and C. A. Doswell III, 2016: Comments on "Double impact: When both tornadoes and flash floods threaten the same place at the same time." *Wea. Forecasting*, **31**, 1715–1721, https://doi.org/10.1175/WAF-D-16-0116.1.

Byers, H. R., and H. R. Rodebush, 1948: Causes of thunderstorms of the Florida Peninsula. *J. Meteor.*, **5**, 275–280, https://doi.org/10.1175/1520-0469(1948)005<0275:COTOTF>2.0.CO;2.

Coffer, B. E., and M. D. Parker, 2015: Impacts of increasing low-level shear on supercells during the early evening transition. *Mon. Wea. Rev.*, **143**, 1945–1969, https://doi.org/10.1175/MWR-D-14-00328.1.

Costa, J. E., 1987: Hydraulics and basin morphometry of the largest flash floods in the conterminous United States. *J. Hydrol.*, **93**, 313–338, https://doi.org/10.1016/0022-1694(87)90102-8.

Craven, J. P., H. E. Brooks, and J. A. Hart, 2004: Baseline climatology of sounding derived parameters associated with deep, moist convection. *Natl. Wea. Dig.*, **28** (1), 13–24.

Creutin, J. D., M. Borga, C. Lutoff, A. Scolobig, I. Ruin, and L. Créton-Cazanave, 2009: Catchment dynamics and social response during flash floods: The potential of radar rainfall monitoring for warning procedures. *Meteor. Appl.*, **16**, 115–125, https://doi.org/10.1002/met.128.

Dalrymple, T., 1937: Major Texas floods of 1935. U.S. Geological Survey Water Supply Paper 796-G, 287 pp.

Doswell, C. A., III, H. E. Brooks, and R. A. Maddox, 1996: Flash flood forecasting: An ingredients-based methodology. *Wea. Forecasting*, **11**, 560–581, https://doi.org/10.1175/1520-0434(1996)011<0560:FFFAIB>2.0.CO;2.

——, C. Ramis, R. Romero, and S. Alonso, 1998: A diagnostic study of three heavy precipitation episodes in the western Mediterranean region. *Wea. Forecasting*, **13**, 102–124, https://doi.org/10.1175/1520-0434(1998)013<0102:ADSOTH>2.0.CO;2.

Duda, J. D., and W. A. Gallus Jr., 2010: Spring and summer midwestern severe weather reports in supercells compared to other morphologies. *Wea. Forecasting*, **25**, 190–206, https://doi.org/10.1175/2009WAF2222338.1.

Edwards, R., A. R. Dean, R. L. Thompson, and B. T. Smith, 2012: Convective modes for significant severe thunderstorms in the contiguous United States. Part III: Tropical cyclone tornadoes. *Wea. Forecasting*, **27**, 1507–1519, https://doi.org/10.1175/WAF-D-11-00117.1.

Ester, M., H.-P. Kriegel, J. Sander, and X. Xu, 1996: A density-based algorithm for discovering clusters in large spatial databases with noise. *KDD-96 Proc. Second Int. Conf. on Knowledge Discovery and Data Mining,* Portland, OR, AIAA, 226–231.

Foote, G., and J. Fankhauser, 1973: Airflow and moisture budget beneath a northeast Colorado hailstorm. *J. Appl. Meteor. Climatol.*, **12**, 1330–1353, https://doi.org/10.1175/1520-0450(1973)012<1330:AAMBBA>2.0.CO;2.

Fritsch, J. M., and R. Carbone, 2004: Improving quantitative precipitation forecasts in the warm season: A USWRP research and development strategy. *Bull. Amer. Meteor. Soc.*, **85**, 955–965, https://doi.org/10.1175/BAMS-85-7-955.

Gill, S. E., J. F. Handley, A. R. Ennos, and S. Pauleit, 2007: Adapting cities for climate change: The role of the green infrastructure. *Built Environ.*, **33**, 115–133, https://doi.org/10.2148/benv.33.1.115.

Gochis, D., and Coauthors, 2015: The great Colorado flood of September 2013. *Bull. Amer. Meteor. Soc.*, **96**, 1461–1487, https://doi.org/10.1175/BAMS-D-13-00241.1.

Gourley, J. J., and Coauthors, 2017: The FLASH project: Improving the tools for flash flood monitoring and prediction across the United States. *Bull. Amer. Meteor. Soc.*, **98**, 361–372, https://doi.org/10.1175/BAMS-D-15-00247.1.

Hapuarachchi, H., Q. Wang, and T. Pagano, 2011: A review of advances in flash flood forecasting. *Hydrol. Processes*, **25**, 2771–2784, https://doi.org/10.1002/hyp.8040.

Herman, G. R., and R. S. Schumacher, 2016: Extreme precipitation in models: An evaluation. *Wea. Forecasting*, **31**, 1853–1879, https://doi.org/10.1175/WAF-D-16-0093.1.

——, and ——, 2018a: "Dendrology" in numerical weather prediction: What random forests and logistic regression tell us about forecasting extreme precipitation. *Mon. Wea. Rev.*, **146**, 1785–1812, https://doi.org/10.1175/MWR-D-17-0307.1.

——, and ——, 2018b: Flash flood verification: Pondering precipitation proxies. *J. Hydrometeor.*, **19**, 1753–1776, https://doi.org/10.1175/JHM-D-18-0092.1.

——, and ——, 2018c: Money doesn't grow on trees, but forecasts do: Forecasting extreme precipitation with random forests. *Mon. Wea. Rev.*, **146**, 1571–1600, https://doi.org/10.1175/MWR-D-17-0250.1.

Hitchens, N. M., and H. E. Brooks, 2013: Preliminary investigation of the contribution of supercell thunderstorms to the climatology of heavy and extreme precipitation in the United States. *Atmos. Res.*, **123**, 206–210, https://doi.org/10.1016/j.atmosres.2012.06.023.

IEM, 2017: Iowa Environmental Mesonet COW: NWS storm based warning verification. Accessed 27 September 2017, https://mesonet.agron.iastate.edu/cow/.

——, 2018: Iowa Environmental Mesonet: ASOS-AWOS-METAR data download. Accessed 5 April 2018, https://mesonet.agron.iastate.edu/request/download.phtml.

James, E. P., and R. H. Johnson, 2010: Patterns of precipitation and mesolow evolution in midlatitude mesoscale convective vortices. *Mon. Wea. Rev.*, **138**, 909–931, https://doi.org/10.1175/2009MWR3076.1.

Jones, T. A., K. M. McGrath, and J. T. Snow, 2004: Association between NSSL mesocyclone detection algorithm-detected vortices and tornadoes. *Wea. Forecasting*, **19**, 872–890, https://doi.org/10.1175/1520-0434(2004)019<0872:ABNMDA>2.0.CO;2.

Kandel, D., A. Western, R. Grayson, and H. Turral, 2004: Process parameterization and temporal scaling in surface runoff and erosion modelling. *Hydrol. Processes*, **18**, 1423–1446, https://doi.org/10.1002/hyp.1421.

Kelsch, M., 2001: Hydrometeorological characteristics of flash floods. *Coping with Flash Floods*, E. Gruntfest and J. Handmer, Eds., Springer, 181–193.

——, E. Caporali, and L. G. Lanza, 2001: Hydrometeorology of flash floods. *Coping with Flash Floods,* E. Gruntfest and J. Handmer, Eds., Springer, 19–35.

Klemp, J. B., 1987: Dynamics of tornadic thunderstorms. *Annu. Rev. Fluid Mech.*, **19**, 369–402, https://doi.org/10.1146/annurev.fl.19.010187.002101.

——, and R. Rotunno, 1983: A study of the tornadic region within a supercell thunderstorm. *J. Atmos. Sci.*, **40**, 359–377, https://doi.org/10.1175/1520-0469(1983)040<0359:ASOTTR>2.0.CO;2.

Legates, D., and T. Deliberty, 1993: Precipitation measurement biases in the United States. *Water Resour. Bull.*, **29**, 855–861, https://doi.org/10.1111/j.1752-1688.1993.tb03245.x.

Lin, Y., and K. E. Mitchell, 2005: The NCEP Stage II/IV hourly precipitation analyses: Development and applications. *19th Conf. on Hydrology*, San Diego, CA, Amer. Meteor. Soc., 1.2, http://ams.confex.com/ams/pdfpapers/83847.pdf.

Maddox, R. A., C. F. Chappell, and L. R. Hoxit, 1979: Synoptic and meso-α-scale aspects of flash flood events. *Bull. Amer. Meteor. Soc.*, **60**, 115–123, https://doi.org/10.1175/1520-0477-60.2.115.

Maples, L. Z., and J. P. Tiefenbacher, 2009: Landscape, development, technology and drivers: The geography of drownings associated with automobiles in Texas floods, 1950–2004. *Appl. Geogr.*, **29**, 224–234, https://doi.org/10.1016/j.apgeog.2008.09.004.

Markowski, P. M., and Y. P. Richardson, 2010: *Mesoscale Meteorology in Midlatitudes*. Wiley-Blackwell, 430 pp.

——, and ——, 2014: The influence of environmental low-level shear and cold pools on tornadogenesis: Insights from idealized simulations. *J. Atmos. Sci.*, **71**, 243–275, https://doi.org/10.1175/JAS-D-13-0159.1.

Marwitz, J. D., 1972: Precipitation efficiency of thunderstorms on the high plains. *J. Rech. Atmos.*, **6**, 367–370.

Michaels, P. J., R. A. Pielke, J. McQueen, and D. Sappington, 1987: Composite climatology of florida summer thunderstorms. *Mon. Wea. Rev.*, **115**, 2781–2791, https://doi.org/10.1175/1520-0493(1987)115<2781:CCOFST>2.0.CO;2.

Mohamadi, M. A., and A. Kavian, 2015: Effects of rainfall patterns on runoff and soil erosion in field plots. *Int. Soil Water Conserv. Res.*, **3**, 273–281, https://doi.org/10.1016/j.iswcr.2015.10.001.

Morin, M. J., and M. D. Parker, 2011: A numerical investigation of supercells in landfalling tropical cyclones. *Geophys. Res. Lett.*, **38**, L10801, https://doi.org/10.1029/2011GL047448.

Nelson, B. R., O. P. Prat, D.-J. Seo, and E. Habib, 2016: Assessment and implications of NCEP Stage IV quantitative precipitation estimates for product intercomparisons. *Wea. Forecasting*, **31**, 371–394, https://doi.org/10.1175/WAF-D-14-00112.1.

Nielsen, E. R., 2019: Insights into extreme short-term precipitation associated with supercells and mesovortices. Ph.D. thesis, Colorado State University, 182 pp.

——, and R. S. Schumacher, 2018: Dynamical insights into extreme short-term precipitation associated with supercells and mesovortices. *J. Atmos. Sci.*, **75**, 2983–3009, https://doi.org/10.1175/JAS-D-17-0385.1.

——, G. R. Herman, R. C. Tournay, J. M. Peters, and R. S. Schumacher, 2015: Double impact: When both tornadoes and flash floods threaten the same place at the same time. *Wea. Forecasting*, **30**, 1673–1693, https://doi.org/10.1175/WAF-D-15-0084.1.

——, ——, ——, ——, and ——, 2016a: Reply to "Comments on 'Double impact: When both tornadoes and flash floods threaten the same place at the same time.'" *Wea. Forecasting*, **31**, 1723–1727, https://doi.org/10.1175/WAF-D-16-0151.1.

——, R. S. Schumacher, and A. M. Keclik, 2016b: The effect of the Balcones Escarpment on three cases of extreme precipitation in central Texas. *Mon. Wea. Rev.*, **144**, 119–138, https://doi.org/10.1175/MWR-D-15-0156.1.

Novak, D. R., C. Bailey, K. Brill, M. Eckert, D. Petersen, R. Rausch, and M. Schichtel, 2011: Human improvement to NWP at the Hydrometeorological Prediction Center. *24th Conf. on Weather and Forecasting/20th Conf. on Numerical Weather Prediction*, Seattle, WA, Amer. Meteor. Soc., 440, https://ams.confex.com/ams/91Annual/webprogram/Paper181989.html.

NWS, 1999: Service assessment: South Texas Floods October 17-22, 1998. National Weather Service, 24 pp., https://www.weather.gov/media/publications/assessments/texasflood98.pdf.

——, 2011: Service assessment: Record floods of greater Nashville: Including flooding in middle Tennessee and western Kentucky, May 1-4, 2010. National Weather Service, 93 pp.

——, 2017: National Weather Service manual 10-950: Definitions and general terminology. Hydrologic Services Program, NWSPD 10-9, National Weather Service, 5 pp., http://www.nws.noaa.gov/directives/sym/pd01009050curr.pdf.

——, 2018: Summary of natural hazard statistics for 2017 in the United States. NOAA/National Weather Service, 3 pp., https://www.nws.noaa.gov/om/hazstats/sum17.pdf.

Pedregosa, F., and Coauthors, 2011: Scikit-learn: Machine learning in Python. *J. Mach. Learn. Res.*, **12**, 2825–2830, http://dl.acm.org/citation.cfm?id=1953048.2078195.

Perica, S., S. Pavlovic, M. St. Laurent, C. Trypaluk, D. Unruh, and O. Wilhite, 2018: Precipitation-frequency atlas of the United States. NOAA Atlas 14, Vol. 11 (Version 2.0: Texas), NOAA, 295 pp., https://www.nws.noaa.gov/oh/hdsc/PF_documents/Atlas14_Volume2.pdf.

Potvin, C. K., K. L. Elmore, and S. J. Weiss, 2010: Assessing the impacts of proximity sounding criteria on the climatology of significant tornado environments. *Wea. Forecasting*, **25**, 921–930, https://doi.org/10.1175/2010WAF2222368.1.

Rhodes, B. C., 2011: PyEphem: Astronomical Ephemeris for Python. Astrophysics Source Code Library, 1112.014, accessed 30 June 2016.

Rotunno, R., and J. B. Klemp, 1982: The influence of the shear-induced pressure gradient on thunderstorm motion. *Mon. Wea. Rev.*, **110**, 136–151, https://doi.org/10.1175/1520-0493(1982)110<0136:TIOTSI>2.0.CO;2.

——, and ——, 1985: On the rotation and propagation of simulated supercell thunderstorms. *J. Atmos. Sci.*, **42**, 271–292, https://doi.org/10.1175/1520-0469(1985)042<0271:OTRAPO>2.0.CO;2.

Saharia, M., P.-E. Kirstetter, H. Vergara, J. J. Gourley, Y. Hong, and M. Giroud, 2017: Mapping flash flood severity in the United States. *J. Hydrometeor.*, **18**, 397–411, https://doi.org/10.1175/JHM-D-16-0082.1.

Schumacher, R. S., and R. H. Johnson, 2005: Organization and environmental properties of extreme-rain-producing meso-scale convective systems. *Mon. Wea. Rev.*, **133**, 961–976, https://doi.org/10.1175/MWR2899.1.

——, and ——, 2009: Quasi-stationary, extreme-rain-producing convective systems associated with midlevel cyclonic circulations. *Wea. Forecasting*, **24**, 555–574, https://doi.org/10.1175/2008WAF2222173.1.

Sharif, H. O., T. L. Jackson, M. M. Hossain, and D. Zane, 2015: Analysis of flood fatalities in Texas. *Nat. Hazards Rev.*, **16** (1), https://doi.org/10.1061/(ASCE)NH.1527-6996.0000145.

Smith, B., J. Smith, M. Baeck, G. Villarini, and D. Wright, 2013: Spectrum of storm event hydrologic response in urban watersheds. *Water Resour. Res.*, **49**, 2649–2663, https://doi.org/10.1002/wrcr.20223.

Smith, J. A., M. L. Baeck, Y. Zhang, and C. A. Doswell III, 2001: Extreme rainfall and flooding from supercell thunderstorms. *J. Hydrometeor.*, **2**, 469–489, https://doi.org/10.1175/1525-7541(2001)002<0469:ERAFFS>2.0.CO;2.

——, A. A. Cox, M. L. Baeck, L. Yang, and P. Bates, 2018: Strange floods: The upper tail of flood peaks in the United States. *Water Resour. Res.*, **54**, 6510–6542, https://doi.org/10.1029/2018WR022539.

——, M. L. Baeck, L. Yang, J. Signell, E. Morin, and D. C. Goodrich, 2019: The paroxysmal precipitation of the desert: Flash floods in the Southwestern United States. *Water Resour. Res.*, https://doi.org/10.1029/2019WR025480, in press.

Smith, T. L., S. G. Benjamin, J. M. Brown, S. Weygandt, T. Smirnova, and B. Schwartz, 2008: Convection forecasts from the hourly updated, 3-km high resolution rapid refresh model. *24th Conf. on Severe Local Storms*, Savannah, GA, Amer. Meteor. Soc., 11.1, https://ams.confex.com/ams/24SLS/techprogram/paper_142055.htm.

Smith, T. M., and Coauthors, 2016: Multi-Radar Multi-Sensor (MRMS) severe weather and aviation products: Initial operating capabilities. *Bull. Amer. Meteor. Soc.*, **97**, 1617–1630, https://doi.org/10.1175/BAMS-D-14-00173.1.

SPC, 2017: Storm Prediction Center: Archive national sector hourly mesoscale analysis. NOAA/SPC, accessed 28 September 2017, https://www.spc.noaa.gov/exper/ma_archive/.

Špitalar, M., J. J. Gourley, C. Lutoff, P.-E. Kirstetter, M. Brilly, and N. Carr, 2014: Analysis of flash flood parameters and human impacts in the US from 2006 to 2012. *J. Hydrol.*, **519**, 863–870, https://doi.org/10.1016/j.jhydrol.2014.07.004.

Stevenson, S. N., and R. S. Schumacher, 2014: A 10-year survey of extreme rainfall events in the central and eastern United States using gridded multisensor precipitation analyses. *Mon. Wea. Rev.*, **142**, 3147–3162, https://doi.org/10.1175/MWR-D-13-00345.1.

Terti, G., I. Ruin, S. Anquetin, and J. J. Gourley, 2017: A situation-based analysis of flash flood fatalities in the United States. *Bull. Amer. Meteor. Soc.*, **98**, 333–345, https://doi.org/10.1175/BAMS-D-15-00276.1.

Thompson, R. L., R. Edwards, J. A. Hart, K. L. Elmore, and P. Markowski, 2003: Close proximity soundings within supercell environments obtained from the rapid update cycle. *Wea. Forecasting*, **18**, 1243–1261, https://doi.org/10.1175/1520-0434(2003)018<1243:CPSWSE>2.0.CO;2.

——, B. T. Smith, J. S. Grams, A. R. Dean, and C. Broyles, 2012: Convective modes for significant severe thunderstorms in the contiguous United States. Part II: Supercell and QLCS tornado environments. *Wea. Forecasting*, **27**, 1136–1154, https://doi.org/10.1175/WAF-D-11-00116.1.

Trapp, R. J., G. R. Marion, and S. W. Nesbitt, 2017: The regulation of tornado intensity by updraft width. *J. Atmos. Sci.*, **74**, 4199–4211, https://doi.org/10.1175/JAS-D-16-0331.1.

Unidata, 2018: THREDDS data server (TDS) version 4.6.2. UCAR/Unidata, Boulder, CO, accessed 15 October 2018, http://doi.org/10.5065/D6N014KG.

Weijenborg, C., J. Chagnon, P. Friederichs, S. Gray, and A. Hense, 2017: Coherent evolution of potential vorticity anomalies associated with deep moist convection. *Quart. J. Roy. Meteor. Soc.*, **143**, 1254–1267, https://doi.org/10.1002/qj.3000.

Woolhiser, D., and D. Goodrich, 1988: Effect of storm rainfall intensity patterns on surface runoff. *J. Hydrol.*, **102**, 335–354, https://doi.org/10.1016/0022-1694(88)90106-0.

Yang, D., B. E. Goodison, J. R. Metcalfe, V. S. Golubev, R. Bates, T. Pangburn, and C. L. Hanson, 1998: Accuracy of NWS 8'' standard nonrecording precipitation gauge: Results and application of WMO intercomparison. *J. Atmos. Oceanic Technol.*, **15**, 54–68, https://doi.org/10.1175/1520-0426(1998)015<0054:AONSNP>2.0.CO;2.

Zhang, J., and Coauthors, 2016: Multi-Radar Multi-Sensor (MRMS) quantitative precipitation estimation: Initial operating capabilities. *Bull. Amer. Meteor. Soc.*, **97**, 621–638, https://doi.org/10.1175/BAMS-D-14-00174.1.